Chemodynamics of newly identified giants with a globular cluster like abundance patterns in the bulge, disk, and halo of the Milky Way

José Fernández-Trincado, Timothy Beers, Baitian Tang, Edmundo Moreno, Angeles Pérez-Villegas, Mario Ortigoza-Urdaneta

Monthly Notices
of the
ROYAL ASTRONOMICAL SOCIETY

MNRAS **488,** 2864–2880 (2019)
Advance Access publication 2019 July 8

doi:10.1093/mnras/stz1848

Chemodynamics of newly identified giants with a globular cluster like abundance patterns in the bulge, disc, and halo of the Milky Way

José G. Fernández-Trincado,[1,2,3★] Timothy C. Beers,[4] Baitian Tang,[5] Edmundo Moreno,[6] Angeles Pérez-Villegas[7] and Mario Ortigoza-Urdaneta[1]

[1]*Instituto de Astronomía y Ciencias Planetarias, Universidad de Atacama, Copayapu 485, Copiapó, Chile*
[2]*Institut Utinam, CNRS UMR6213, Univ. Bourgogne Franche-Comté, OSU THETA , Observatoire de Besançon, BP 1615, 25010 Besançon Cedex, France*
[3]*Departamento de Astronomía, Casilla 160-C, Universidad de Concepción, Concepción, Chile*
[4]*Department of Physics and JINA Center for the Evolution of the Elements, University of Notre Dame, Notre Dame, IN 46556, USA*
[5]*School of Physics and Astronomy, Sun Yat-sen University, Zhuhai 519082, China*
[6]*Instituto de Astronomía, Universidad Nacional Autónoma de México, Apdo. Postal 70264, México D.F., 04510, México*
[7]*Universidade de São Paulo, IAG, Rua do Matão 1226, Cidade Universitária, São Paulo 05508-900, Brazil*

Accepted 2019 June 28. Received 2019 June 27; in original form 2019 April 10

ABSTRACT

The latest edition of the APOGEE-2/DR14 survey catalogue and the first `Payne` data release of APOGEE abundance determinations by Ting et al. are examined. We identify 31 previously unremarked metal-poor giant stars with anomalously high levels of [N/Fe] abundances, which is not usually observed among metal-poor stars in the Milky Way. We made use of the Brussels Automatic Stellar Parameter (BACCHUS) code to re-derive manually the chemical abundances of 31 field stars in order to compile the main element families, namely the light elements (C, N), a-elements (O, Mg, Si), iron-peak element (Fe), s-process elements (Ce, Nd), and the light odd-*Z* element (Na, Al). We have found all these objects have a [N/Fe] $\gtrsim +0.5$, and are thus identified here as nitrogen-rich stars. An orbital analysis of these objects revealed that a handful of them shares the orbital properties of the bar/bulge, and possibly linked to tidal debris of surviving globular clusters trapped into the bar component. Three of the 31 stars are actually halo interlopers into the bulge area, which suggests that halo contamination is not insignificant when studying N-rich stars found in the inner Galaxy, whereas the rest of the N-rich stars share orbital properties with the halo population. Most of the newly identified population exhibits chemistry similar to the so-called *second-generation* globular cluster stars (enriched in aluminum, [Al/Fe] $\gtrsim +0.5$), whereas a handful of them exhibit lower abundances of aluminum, [Al/Fe] $< +0.5$, which are thought to be chemically associated with the *first generation* of stars, as seen in globular clusters, or compatible with origin from a tidally disrupted dwarf galaxy.

Key words: stars: abundances – stars: chemically peculiar – Galaxy: abundances – Galaxy: bulge – globular clusters: general – Galaxy: halo.

1 INTRODUCTION

The advent of large spectroscopic surveys such as APOGEE (Majewski et al. 2017) and its capability to measure the atmospheric composition of ∼176 000 giants distributed homogeneously over much of the Milky Way (bulge, disc, and halo), and especially designed to observe where extinction by dust is significantly higher, has opened up a new panoramic window on our Galaxy, providing the precise chemical abundance of more than 23 chemical species (e.g. C, N, O, Na, Mg, Al, Si, P, S, K, Ca, Ti, V, Cr, Mn, Co, Ni, Cu, Ge, Rb, Nd, Ce, and Yb).

The detailed and unprecedented precision of most of the stellar elemental abundances provided in the *H* band (λ1.5–1.7 μm) has enabled the discovery of giants with unusual abundance patterns throughout the Galaxy. For example, Martell et al. (2016), Fernández-Trincado et al. (2016b, 2017), Schiavon et al. (2017a), Kemp et al. (2018), Koch, Grebel & Martell (2019), Pereira et al. (2019b), Pereira, Drake & Roig (2019a), Fernández-Trincado et al. (2019a), and Fernández-Trincado et al. (2019b) have identified a unique collection of stars in the Galactic field that exhibits light-/heavy-element abundance ratios above the Galactic levels. Most of the APOGEE spectra have been re-analyzed manually in the works

★ E-mail: jose.fernandez@uda.cl, jfernandez@obs-besancon.fr, jfernandezt87@gmail.com

above, with the conclusion that a significant fraction of giants fell within the bounds of the chemically anomalous stars unique to Galactic and/or extragalactic globular cluster environments. Their number has become increased in recent years (see Recio-Blanco et al. 2017; Kemp et al. 2018; Tang et al. 2019), thanks to other extensive spectroscopic surveys such as LAMOST, which obtained low-resolution spectra (Cui et al. 2012; Deng et al. 2012; Luo et al. 2012; Zhao et al. 2012), and the Gaia-ESO survey, with both medium- and high-resolution spectra (Gilmore et al. 2012; Randich et al. 2013). So far, these results demonstrate that those inhomogeneities appear to occur in other star-formation environments. Such stars have received significant attention in recent years, primarily because they are considered as evaporated from stellar clusters, and as such, play an important role in deciphering the early history of the Galactic formation process (Martell & Grebel 2010; Martell et al. 2011; Carollo et al. 2013; Fernández-Trincado et al. 2015a,b, 2016a; Helmi et al. 2018; Khoperskov et al. 2018; Minniti et al. 2018; Ibata, Malhan & Martin 2019), as well as providing clues on the mechanism responsible for the ejection from stellar clusters and its relation with chemical peculiarity (e.g. Pereira et al. 2017, 2019b).

Often, stars with 'anomalous chemistry' have been qualitatively linked to the so–called *second-generation*[1] globular cluster stars, which clearly exhibit enhanced N, Na, and Al and depleted C, Mg, and O abundances with respect to field stars at the same metallicity (e.g. Bastian & Lardo 2018), however, this terminology is ambiguous in multiple ways. The implicit assumption that the unusual abundance patterns result after the chemically mundane stars and have been enriched by a previous generation has not been fully demonstrated. Here, we refer to the stars with peculiar chemical composition as enriched, and the stars having field-like abundances as primordial.

Furthermore, it is now firmly established that carbon-depleted ([C/Fe] $\lesssim +0.15$) giants beyond the metal-poor tail ([Fe/H] $\lesssim -0.7$) of the thick disc with N enrichment ([N/Fe] $\gtrsim +0.5$, hereafter N-rich stars) are found throughout the Milky Way, and owe their unusual elemental abundances to rare astrophysical events or nucleosynthetic pathways in different environments (Mészáros et al. 2015; Schiavon et al. 2017b; Masseron et al. 2019; Fernández-Trincado et al. 2018, 2019a). On the other hand, beyond the intrinsic value of identifying the mechanism responsible for the unusual abundance patterns, which are still far from being understood, the exclusive chemistry of such stars is essential to more broadly improve our understanding of the chain of physical processes experienced by the Milky Way from early. However, the census of chemically anomalous N-rich stars across the Milky Way is still far from complete, especially beyond the bulge regions. Recently, Martell et al. (2016) and Fernández-Trincado et al. (2016b, 2017, 2019a) reported the discovery of 18 new N-rich stars in the bulge, disc, and inner halo of the Milky Way. This work reports the discovery of other 31 new N-rich stars in the bulge, disc, and inner halo.

Here we revisit the APOGEE spectra to conduct the largest updated census of N-rich stars throughout the Milky Way. Furthermore, the current version of the APOGEE Stellar Parameters and Chemical Abundance Pipeline (ASPCAP; García Pérez et al. 2016) does not measure the s-process elements, but these are measurable from Ce II and Nd II lines (Hasselquist et al. 2016; Cunha et al. 2017) in the observed spectral window, and carry important information about stellar nucleosynthesis along the RGB and AGB. Here we provide, for the first time, measures of the neutron-capture element Ce II (Cunha et al. 2017) for some of these candidates. In particular, studies of s-process elements provide strong evidence either for or against the uniqueness of the progenitor stars to stellar systems. In Section 2 we outline our methods to identify candidates enhanced in nitrogen ([N/Fe] $\gtrsim +0.5$) and depleted in carbon ([C/Fe] $\lesssim +0.15$). In Section 3 we discuss our results, and in Section 4 we present our concluding remarks.

[1]Here, we refer to second generation to the groups of stars showing enhanced N and Al, and depleted C and O abundances, with respect to other field stars at the same metallicity [Fe/H].

2 DATA AND METHODS

2.1 Targets analysed

The sample analysed in this work consists of red giants from the 14th data release of SDSS (DR14; Abolfathi et al. 2018; Holtzman et al. 2018; Jönsson et al. 2018) of the APOGEE-2 survey (Majewski et al. 2017), which has obtained high-resolution ($R \sim 22\,500$) spectra of ∼270 000 stars in the H-band (∼λ1.5–1.7 μm), using the 300-fiber cryogenic spectrograph installed on the 2.5 m telescope (Gunn et al. 2006) at the Apache Point Observatory, as part of the Sloan Digital Sky Survey IV (Blanton et al. 2017). We refer the reader to Zasowski et al. (2013, 2017) for full details regarding the targeting strategies for APOGEE and APOGEE-2, and Nidever et al. (2015), Zamora et al. (2015), Holtzman et al. (2015), and García Pérez et al. (2016) for more details concerning data reduction of the APOGEE spectra, determination of radial velocities, atmospheric parameters, and stellar abundances, respectively.

In this work, we have selected a sub-sample of metal-poor ([Fe/H] $\lesssim -0.7$) red giants in the first `Payne` data release of APOGEE abundances (Ting et al. 2019, hereafter Payne-APOGEE) that satisfy the following quality cuts to further ensure reliable parameter/abundance derivation:

- S/N > 70
- 3000 K $< T_{\rm eff} <$ 5500 K
- log g < 3.6
- `quality_flags` = good

The `Payne` routine (see Ting et al. 2019) simultaneously derives best-fitting values for all atmospheric parameters and abundances using neural networks, with the parameter space of the training set restricted to [Fe/H] $\gtrsim -1.5$. For the same reason as in Fernández-Trincado et al. (2016b, 2017, 2019a) and Schiavon et al. (2017a), we remove stars with [C/Fe] > +0.15, because such stars are not typically found in globular clusters, and we want to minimize the contamination by objects such as CH stars (e.g. Karinkuzhi & Goswami 2015), leaving us with a total of 6289 giants with metallicities in the range $-1.5 <$ [Fe/H] < -0.7.

To search for outliers in the [N/Fe]-[Fe/H] abundance plane (see Fig. 1), we binned in [Fe/H] space (0.05 dex bins), and by fitting a 5th-order polynomial to the bulk of the stars, select stars that deviate from the fit by more than $\gtrsim 2.5\sigma$ from that curve as nitrogen-rich red giants, i.e. we label all stars with nitrogen abundance more than ∼0.4 dex above the mean at a fixed metallicity as 'N-rich'. The bins were chosen to ensure that at least 200 stars occupied each bin (see inner label numbers in Fig. 1). On the side of caution, we checked for the presence of a bias that could have been introduced by the choice of a high-order polynomial fit. We also found that fitting a 2nd-order polynomial does not affect our results and conclusions in any important way.

In a similar way as described in Schiavon et al. (2017a), we note that over a more limited metallicity range, a sixth-order polynomical

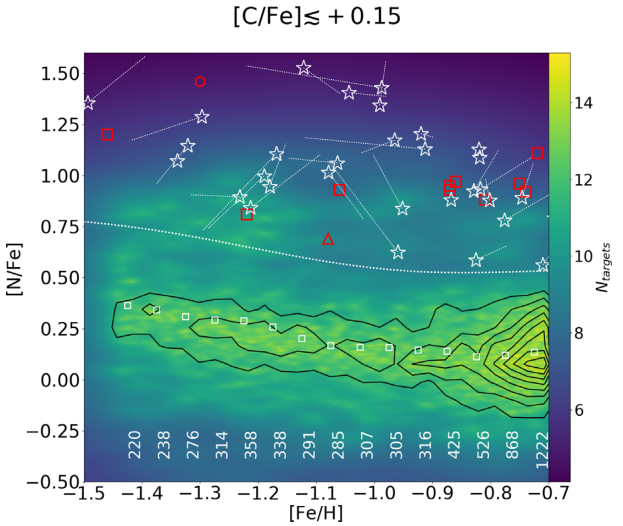

Figure 1. Kernel Density Estimate smoothed distribution of [N/Fe] and [Fe/H] for Payne-APOGEE stars, with the black contours showing the density of objects in the main body of N-normal stars ([N/Fe] $\lesssim +0.5$). The number of stars of each bin is shown at the center of the bin at the lower portion of the plot, while the white unfilled square symbols show the mean value of [N/Fe] by bin. The white star symbols are of newly discovered N-rich stars in this study, manually re-analyzed adopting a simple line-by-line approach with the BACCHUS code, with white tiny dotted lines showing the sensitivity to photometry stellar parameters (see the text). The same field sample is compared to a sample of previously identified N-rich stars (red unfilled symbols) from the APOGEE survey and manually inspected line-by-line: *hexagon*–Fernández-Trincado et al. (2016b), *squares*–Fernández-Trincado et al. (2017), and *triangles*–Fernández-Trincado et al. (2019a).

also captures the mean behaviour of our data set well, which includes stars located towards the disc, bulge, and halo, simultaneously. This is the first time that such global feature is evaluated across the Milky Way (disc+halo + bulge) to homogeneously identify such anomalous stars. The initial sample contained about 300 N-rich candidates, according to the [N/Fe] versus [Fe/H] abundance plane from Payne-APOGEE determinations. These stars have high [N/Fe] ratios ($\gtrsim +0.5$ dex).

There was expected to be some contamination by star clusters and other previously reported outliers, which we remove from our sample. We found that 177 out of 284 stars are confirmed cluster stars (Fernández-Trincado et al. 2018; Masseron et al. 2019), while 31 out of 284 stars are known N-rich stars previously reported in Martell et al. (2016), Fernández-Trincado et al. (2016b), Schiavon et al. (2017a), Fernández-Trincado et al. (2017), and Fernández-Trincado et al. (2019a). This yields 79 stars that are previously overlooked nitrogen-rich objects relative in the final data set. For reasons that are explained below, we remove 48 of those stars from our final analysis.

Fig. 1 shows our final data set in the [N/Fe]-[Fe/H] plane against the giants that have unusually high N abundances. After applying a number of stringent selection criteria, this yielded the discovery of 31 further N-rich stars (bona fide chemically anomalous giants), adding to the ∼100 such objects out of ∼7000 regular disc (thick) and halo stars from previous studies.

2.2 Stellar parameters and chemical abundance measurements

In order to examine the reliability of these high-[N/Fe] outliers, we performed a careful inspection of each APOGEE spectrum. We made use of the Brussels Automatic Stellar Parameter (BACCHUS) code (Masseron, Merle & Hawkins 2016) to derive the metallicity, broadening parameters, and chemical abundances for the newly identified N-rich sample, making a careful line selection as well as providing abundances based on a line-by-line differential approach.

BACCHUS relies on the radiative transfer code Turbospectrum (Alvarez & Plez 1998; Plez 2012) and the MARCS model atmosphere grid (Gustafsson et al. 2008). For each element and each line, the abundance determination proceeds as in Hawkins et al. (2016), Fernández-Trincado et al. (2017, 2018), and Fernández-Trincado et al. (2019a), and summarized here for guindance: (i) a spectrum synthesis, using the full set of (atomic and molecular) lines, is used to find the local continuum level via a linear fit; (ii) cosmic and telluric rejections are performed; (iii) the local S/N is estimated; (iv) a series of flux points contributing to a given absorption line is automatically selected; and (v) abundances are then derived by comparing the observed spectrum with a set of convolved synthetic spectra characterized by different abundances. Four different abundance determinations are used: (i) line-profile fitting; (ii) core line-intensity comparison; (iii) global goodness-of-fit estimate; and (iv) equivalent width comparison. Each diagnostic yields validation flags. Based on these flags, a decision tree then rejects the line or accepts it, keeping the best-fitting abundance. We adopted the χ^2 diagnostic as it is the most robust. However, we store the information from the other diagnostics, including the standard deviation, between all four methods.

The linelist used in this work is the latest internal DR14 atomic/molecular linelist (linelist.20170418). For a more detailed description of these lines, we refer the reader to a forthcoming paper (Holtzman et al., in preparation). The current version of ASPCAP/DR14 and the Payne routine do not determine the s-process elements (Nd II and Ce II). Thus, we determine, for the first time, these elements in our target stars, adopting the linelists provided in Hasselquist et al. (2016) and Cunha et al. (2017).

For the light elements, a mix of heavily CN-cycled and α-poor MARCS models was used, as well as the same molecular lines adopted by Smith et al. (2013), was employed to determine the C, N, and O abundances. In addition, we have adopted the C, N, and O abundances that satisfy the fitting of all molecular lines consistently; i.e. we first derive ^{16}O abundances from ^{16}OH lines, then derive ^{12}C from ^{12}C^{16}O lines and ^{14}N from ^{12}C^{14}N lines, and the CNO abundances are derived several times to minimize the OH, CO, and CN dependences (see e.g. Smith et al. 2013; Fernández-Trincado et al. 2016b, 2017, 2018, 2019a).

Atmospheric parameters from spectroscopy: In order to provide a consistent chemical analysis, we re-determine the chemical abundances assuming as input the effective temperature ($T_{\rm eff}$), surface gravity (log g), and metallicity ([Fe/H]) as derived by the Payne-APOGEE runs (see e.g. Ting et al. 2019).

Atmospheric parameters from photometry: We also applied a simple approach of fixing $T_{\rm eff}^{\rm pho}$ and log g to values determined independently of spectroscopy, in order to check for any significant deviation in the chemical abundances. For this, the photometric effective temperatures were calculated from the $J_{\rm 2MASS} - K_{s,\rm 2MASS}$ colour relation using the methodology presented in González Hernández & Bonifacio (2009). Photometry is extinction corrected using the Rayleigh Jeans Color Excess method (e.g. Majewski, Zasowski & Nidever 2011). The results are listed in Table 1. We estimate surface gravity from 10 Gyr PARSEC (Bressan et al. 2012) isochrones, as illustrated in Fig. 2, since 10 Gyr is the typical age of Galactic GCs (Harris 1996). The mean elemental abundances derived with the BACCHUS code are listed in Table 1.

Table 1. Adopted atmospheric parameters of our target stars, radial velocity scatter information ($RV_{SCATTER}$), and frequency of observation per object (N_{visits}), the mean elemental abundances derived for our target stars using the 'abund' module in BACCHUS code, adopting the atmospheric parameters from Payne-APOGEE (abundances labeled as $[X/Fe]_{sp}$), and atmospheric parameters from photometry and isochrones (abundances labeled as $[X/Fe]_{pho}$).

APOGEE−ID	Payne [Fe/H]	$J-K$	$\langle A_K^{WISE}\rangle$	$E(B-V)$	T_{eff}^{pho}	$\log^{iso} g$	Payne T_{eff}	Payne $\log g$	$RV_{SCATTER}$	N_{visits}	[Fe/H]	[C/Fe]	[N/Fe]	[O/Fe]	[Mg/Fe]	[Al/Fe]	[Si/Fe]	[Ce/Fe]	[Nd/Fe]	[Na/Fe]	[Fe/H]	[C/Fe]	[N/Fe]	[O/Fe]	[Mg/Fe]	[Al/Fe]	[Si/Fe]	[Ce/Fe]	[Nd/Fe]	[Na/Fe]	Classification
	K	mag (2MASS)	mag		K	dex	K	dex	km s^{-1}		sp	sp	sp	sp	sp	sp	sp	sp	sp	sp	pho	pho	pho	pho	pho	pho	pho	pho	pho	pho	
2M01121802 + 6219193	−1.421	1.044	0.336	...	...	...	4931.82	2.253	0.08	3	−1.34	− 0.03	1.07	0.64	0.12	...	...	<0.42	...	...	...	...	...	...	...	...	...	...	...	...	*FG-like/dGs*
2M02000451 − 0229333	−1.289	0.699	0.045	0.028	4614.73	1.499	4738.89	2.032	0.19	6	−1.23	− 0.03	0.89	0.55	0.18	−0.02	0.32	0.64	...	...	−1.32	−0.17	0.90	0.48	0.22	−0.02	0.28	0.35	...	...	*FG-like/dGs*
2M06273068 − 0440140	−0.797	0.798	0.151	0.420	5103.98	2.938	4752.06	2.16	0.07	3	−0.69	− 0.29	0.79	0.35	0.05	0.19	0.26	0.24	0.83	...	−0.65	−0.08	1.10	0.77	−0.09	0.15	0.14	0.67	...	...	*FG-like/dGs*
2M11062158 − 0712222	−0.893	0.572	0.042	0.038	5039.55	2.673	4820.19	2.416	0.14	5	−0.82	− 0.22	0.93	0.33	0.03	0.09	0.21	0.23	...	...	−0.73	−0.19	1.09	0.53	0.01	0.10	0.16	0.17	...	...	*FG-like/dGs*
2M11514952 + 2015267	−1.225	0.644	0.071	0.048	4822.40	1.970	4726.44	2.235	0.06	3	−1.21	− 0.08	0.84	0.40	0.18	0.07	0.38	0.05	...	...	−1.09	−0.40	1.10	0.56	0.30	0.11	0.29	−0.03	...	...	*FG-like/dGs*
2M12010401 − 0058306	−1.009	0.612	0.033	0.024	4880.99	2.247	4779.53	2.461	1.52	3	−1.12	− 0.00	1.53	0.48	0.21	0.09	0.44	1.00	...	...	−1.06	0.12	1.40	0.59	0.29	0.12	0.33	0.92	...	...	*FG-like/dGs*
2M12042878 + 1949535	−1.384	0.645	0.026	0.022	4767.64	1.707	4824.94	2.208	0.15	3	−1.32	< − 0.19	1.15	0.59	0.27	0.31	0.24	0.37	1.11	...	−1.37	...	0.96	0.61	0.35	0.33	0.33	<0.22	...	...	*FG-like/dGs*
2M12092246 + 0545111	−1.289	0.762	0.107	0.016	4412.57	1.131	4599.0	1.83	0.44	4	−1.17	− 0.51	1.11	0.29	0.02	0.74	0.22	<0.22	...	...	−1.29	−0.44	0.73	0.08	0.07	0.70	0.23	0.20	...	...	*SG-like*
2M12444724 − 0207405	−0.931	0.615	0.067	0.033	4885.23	2.342	4859.61	2.439	0.15	3	−0.92	− 0.27	1.2	0.42	0.09	0.39	0.36	0.32	<0.76	...	−0.90	−0.33	1.19	0.43	0.11	0.36	0.21	0.28	<0.86	...	*FG-like/dGs*
2M13481355 − 0040484	−1.014	0.698	0.055	0.028	4618.69	1.731	4914.06	2.445	0.21	4	−0.91	< − 0.28	1.13	0.61	0.12	0.19	0.25	...	...	...	−1.12	<−0.47	1.18	0.36	0.22	0.17	0.27	0.32	...	...	*FG-like/dGs*
2M13503160 + 4411389	−1.082	0.499	0.061	0.012	5250.21	3.114	5142.27	3.201	0.17	3	−0.99	− 0.33	1.34	...	0.01	0.90	0.23	...	...	...	−0.98	−0.23	1.56	<1.06	0.05	0.92	0.26	...	...	...	*SG-like*
2M14082554 + 4711096	−1.118	0.533	0.053	0.015	5128.05	2.719	5103.23	2.716	0.0	1	−1.08	< − 0.26	1.01	0.51	0.18	−0.01	0.32	<−0.02	<1.03	...	−1.02	−0.01	0.79	0.53	0.16	0.01	0.26	...	<1.01	...	*FG-like/dGs*
2M14582162 + 4117544	−1.012	0.876	0.091	0.013	4128.17	0.857	4204.34	1.434	0.0	1	−0.96	− 0.42	0.62	0.24	0.08	0.16	0.17	0.24	<0.28	...	−1.08	−0.51	1.08	0.28	0.08	0.11	0.19	0.14	<0.33	...	*FG-like/dGs*
2M15082716 + 6710075	−1.302	0.812	0.038	0.033	4309.77	0.947	4186.79	1.355	0.8	26	−1.49	0.02	1.36	0.58	−0.33	...	0.16	0.48	...	...	−1.39	−0.16	1.58	0.82	0.04	...	0.10	<0.26	...	...	*FG-like/dGs*
2M15183589 + 0027100	−1.217	0.769	0.095	0.058	4468.69	1.317	4444.12	1.643	0.35	13	−1.18	− 0.33	0.95	0.25	0.11	0.16	0.16	0.17	...	...	−1.15	−0.57	1.16	0.29	0.21	0.20	0.25	0.07	...	...	*FG-like/dGs*
2M15193208 + 0025293	−0.76	0.718	0.089	0.061	4625.32	1.916	4551.84	2.092	0.09	7	−0.80	0.02	0.88	0.38	0.26	0.24	0.59	0.25	...	<0.30	−0.81	−0.01	0.98	0.49	0.33	0.27	0.29	0.05	...	<0.33	*FG-like/dGs*
2M15195065 + 0221533	−0.777	0.679	0.07	0.041	4701.46	2.058	4583.81	1.918	0.0	1	−0.83	− 0.03	0.59	0.50	0.18	0.18	0.67	0.16	...	...	−0.77	−0.00	0.65	0.62	0.18	0.20	0.36	0.16	...	...	*FG-like/dGs*
2M15535831 + 4333280	−1.256	0.675	0.108	0.013	4656.55	1.576	4835.53	2.118	0.34	4	−1.19	...	0.99	0.25	−0.43	1.07	0.54	0.38	<0.84	...	−1.29	...	0.74	0.13	−0.42	1.07	0.51	0.32	...	...	*SG-like*
2M16362792 + 3901180	−0.842	0.668	0.055	0.018	4694.92	2.046	4628.36	2.247	0.04	2	−0.75	− 0.22	0.89	0.27	−0.02	0.07	0.27	0.25	...	...	−0.73	−0.31	1.06	0.43	0.09	0.07	0.18	0.14	...	...	*FG-like/dGs*
2M16464310 + 4731033	−1.013	0.842	0.093	0.021	4221.58	1.023	4497.21	1.729	0.37	12	−0.99	− 0.51	1.43	0.25	0.11	0.84	0.33	1.13	<0.96	...	−1.22	−0.66	1.54	0.07	...	0.49	0.36	<0.64	...	...	*SG-like*
2M17294680 − 2644220	−0.912	1.486	0.493	...	...	...	4486.78	1.743	0.25	2	−0.87	− 0.38	0.88	0.42	0.22	0.24	0.32	0.22	...	...	...	...	...	...	...	...	...	...	...	...	*FG-like/dGs*
2M18022601 − 3106232	−0.835	0.977	0.326	...	...	...	4642.16	1.829	0.27	7	−0.82	− 0.41	1.13	0.24	0.34	0.74	0.67	0.21	0.75	...	...	...	...	...	...	...	...	...	...	...	*SG-like*

Table 1 – *continued*

APOGEE−ID	Payne [Fe/H]	$J-K$	$\langle A_K^{WISE}\rangle$	$E(B\text{-}V)$	$T_{\rm eff}^{\rm pho}$	$\log^{\rm iso} g$	Payne $T_{\rm eff}$	Payne $\log g$	$RV_{\rm SCATTER}$	$N_{\rm visits}$	[Fe/H]	[C/Fe]	[N/Fe]	[O/Fe]	[Mg/Fe]	[Al/Fe]	[Si/Fe]	[Ce/Fe]	[Nd/Fe]	[Na/Fe]	[Fe/H]	[C/Fe]	[N/Fe]	[O/Fe]	[Mg/Fe]	[Al/Fe]	[Si/Fe]	[Ce/Fe]	[Nd/Fe]	[Na/Fe]	Classification
	K	mag (2MASS)	mag		K	dex	K	dex	km s^{-1}		sp	sp	sp	sp	sp	sp	sp	sp	sp	sp	pho	pho	pho	pho	pho	pho	pho	pho	pho	pho	
2M18110406 − 2602142	−0.713	1.117	0.19	...	...	...	4418.24	1.752	0.0	1	−0.82	− 0.23	1.09	0.22	0.18	0.46	0.58	0.40	...	...	...	...	...	...	...	...	...	...	...	...	*FG-like/dGs*
2M18200243 + 0156016	−0.736	1.168	0.322	0.710	4570.84	1.902	4047.75	1.449	0.16	3	−0.71	− 0.07	0.56	0.34	0.09	−0.07	0.22	−0.19	...	...	−0.56	−0.08	1.18	1.17	0.19	0.20	0.25	0.10	...	...	*FG-like/dGs*
2M18461977 − 3021506	−1.002	0.933	0.156	0.197	4278.82	1.124	4234.47	1.584	0.0	1	−0.95	− 0.27	0.84	0.26	0.04	0.13	0.22	0.35	...	<0.04	−1.00	−0.41	1.10	0.45	0.08	0.15	0.21	0.31	...	<0.09	*FG-like/dGs*
2M18472793 − 3033242	−1.156	0.783	0.101	0.173	4640.83	1.628	4647.83	1.891	0.0	1	−1.06	...	1.06	0.38	0.28	0.58	0.46	0.10	...	...	−1.15	...	1.08	0.47	0.18	0.45	0.28	0.10	...	...	*SG-like*
2M18502108 − 2923442	−1.023	0.832	0.152	0.162	4484.83	1.490	4598.75	1.866	0.0	1	−0.97	− 0.27	1.17	0.46	0.30	0.66	0.53	0.37	...	...	−1.02	−0.30	1.11	0.37	0.38	0.68	0.52	0.24	...	...	*SG-like*
2M19004420 + 4421082	−1.079	0.658	0.088	0.069	4823.72	2.052	4813.71	2.332	0.16	3	−1.04	− 0.46	1.4	0.38	0.13	0.26	0.33	0.67	0.70	...	−0.98	−0.49	1.39	0.38	0.22	0.31	0.28	0.56	...	...	*FG-like/dGs*
2M20124750 + 1818007	−0.863	0.763	0.157	0.237	4827.49	2.216	4645.88	2.231	0.22	6	−0.83	− 0.07	0.92	0.25	0.23	0.30	0.43	0.17	...	...	−0.79	−0.06	1.13	0.54	0.25	0.34	0.20	0.17	...	...	*FG-like/dGs*
2M21181769 + 0946422	−1.357	0.783	0.116	0.049	4412.88	1.047	4624.36	1.525	0.0	1	−1.30	− 0.52	1.29	0.57	0.14	0.26	0.32	0.25	...	<0.85	−1.42	−0.55	1.17	0.34	0.20	0.25	0.35	0.18	...	<0.47	*FG-like/dGs*
2M22015914 + 1543129	−0.795	0.566	0.045	0.049	5086.80	2.893	4744.41	2.631	0.26	4	−0.78	− 0.03	0.78	0.22	0.20	0.30	0.32	<0.21	...	...	−0.64	0.07	0.99	0.63	0.27	<0.19	0.28	<0.10	...	...	*FG-like/dGs*

Note: The Solar reference abundances are from Asplund, Grevesse & Sauval (2005) and Grevesse et al. (2015) for Ce II and Nd II. The BACCHUS pipeline was used to derive the broadening parameters, metallicity, and chemical abundances. Table 1 is published in its entirety via CDS. A portion is shown here for guidance regarding its form and content.

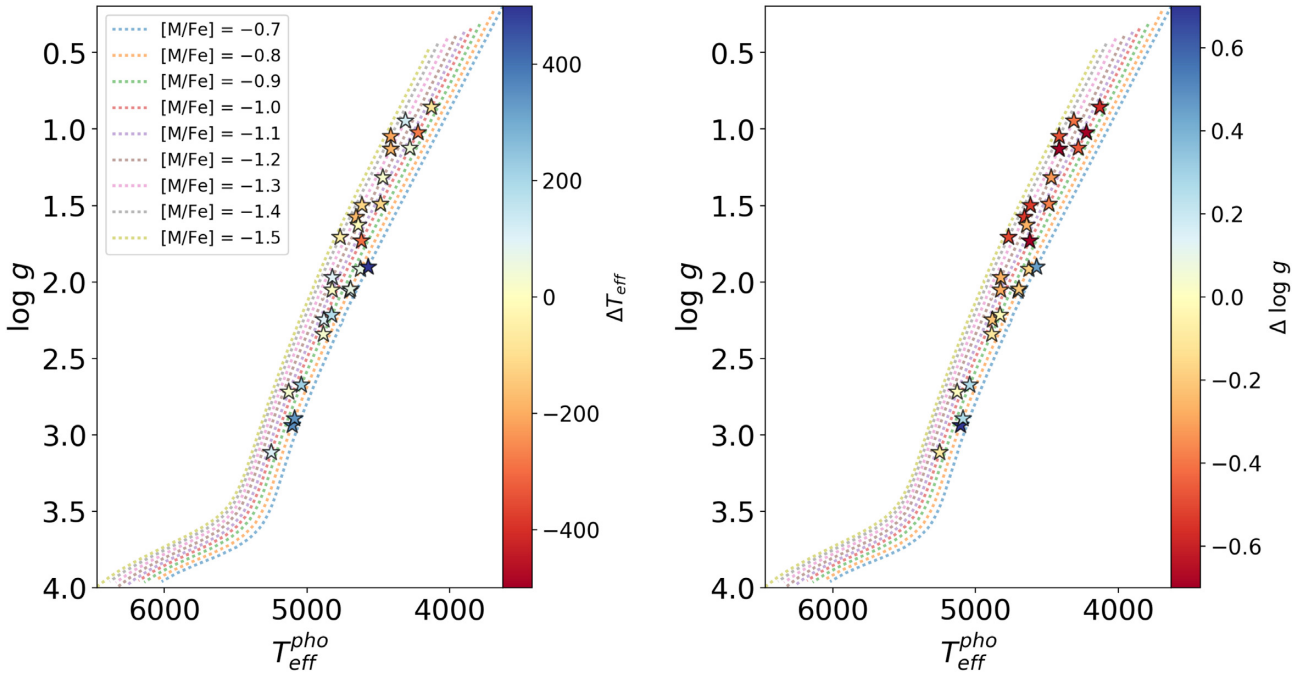

Figure 2. Location of the N-rich stars (star symbols) analyzed in this work in the log g – $T_{\rm eff}$ plane. The symbols are colour-coded by the differences between the photometric and Payne temperatures, $\Delta\ T_{\rm eff} = T_{\rm eff}^{\rm pho} - T_{\rm eff}^{\rm Payne}$, and the log g from 10 Gyr isochrones and Payne log g, $\Delta\log g = \log g - \log g^{\rm Payne}$.

Fig. 2 compares the difference between the adopted atmospheric parameters as the stars ascend the giant branch. Fig. 3 shows the difference of the derived chemical species from the BACCHUS pipeline for both adopted atmospheric parameters. The same figure indicates that small systematic differences are present between the spectroscopic and atmospheric parameters. However, for a few stars, the Payne-APOGEE raw temperature higher than $\gtrsim$5000 K and lower than $\lesssim$3500 K in metal-poor stars showed significant, 200–400 K offsets, compared to photometry along with significant surface gravity (0.25–0.7 dex) offsets at the same temperature range, and are thus expected to display large scatter in the abundance analysis, as seen in rows 2, 3, 4, and 5 in Fig. 3, which may be the reason for the large scatter in [N/Fe], [O/Fe], [Na/Fe], [Ce II/Fe], and [Nd II/Fe]. It is important to note that BACCHUS recovers the [Fe I/H] abundance ratios of these stars within 0.09 dex for both photometric and spectroscopic temperatures. The adoption of a purely photometry temperature scale enables us to be somewhat independent of the Payne-APOGEE pipeline and the APOGEE/ASPCAP pipeline, which gives important comparison data for future pipeline validation. The final results presented in this paper are based on the spectroscopic atmospheric parameters provided by Payne-APOGEE, and are used to estimate our final errors (listed in Table 3).

Incidence of false detections: A cautionary note is in order before proceeding with the analysis. Once the atmospheric parameters are determined, for each star the selected $^{12}C^{14}N$ lines were visually inspected to ensure that the spectral fit was adequate. If the lines were not well-reproduced by the synthesis, it was rejected. In addition, for a substantial fraction of our target stars, the $^{12}C^{14}N$ lines were also rejected if they were flagged as problematic by the BACCHUS pipeline, i.e. they were strongly blended or too weak in the spectra of stars with the typical $T_{\rm eff}$ and metallicity of the N-rich sample to deliver reliable [N/Fe] abundances. This indicates, as confirmed by visual inspection of 48 out of 79 stars in our sample, that the spectral fits are of poor quality, or that the stellar parameters are unreliable or both, suggesting that the abundances for these stars cannot be relied on. In this way, 48 stars were identified as false detections, leaving us with a grand total of 31 newly identified reliable N-rich field stars (white unfilled 'star' symbols), as illustrated in Fig. 1. Fig. 4 shows examples for a portion of the observed APOGEE spectra in the region around the strong $^{12}C^{14}N$ bands for our 31 stars, while Fig. 5 shows 12 examples of false detections confirmed by visual inspection, and the spectral fits are of poor quality and the stellar parameters are unreliable, suggesting that the abundances for these stars cannot be relied on. Fig. 6 shows a comparison between the spectra of a N-rich and a N-normal star in the relevant wavelength range containing the $^{12}C^{14}N$ bands. The N-rich star has remarkably stronger $^{12}C^{14}N$ bands which, in view of the similarity between the two stars in all the other relevant parameters, can only mean that it has a much higher nitrogen abundance.

3 RESULTS AND DISCUSSION

3.1 Chemical signatures

In this subsection, we discuss the individual abundance ratios and trends, as a function of metallicity, for the 31 newly identified N-rich stars.

Fig. 7 shows the distribution of [Al/Fe], [N/Fe], [Mg/Fe], [Si/Fe], and [Fe/H] for all stars that made it through the quality criteria discussed in Section 2.1. These elements were chosen because 'migrants' from globular clusters exhibit clear deficiencies and enrichments in these elemental abundances as compared to most stars in Milky Way (Martell et al. 2016; Fernández-Trincado et al. 2016b, 2017; Schiavon et al. 2017a). Most obvious in this plot are the high-[N/Fe] outliers with [N/Fe] $\gtrsim +0.5$, nominally corresponding to a chemically anomalous population, commonly associated with

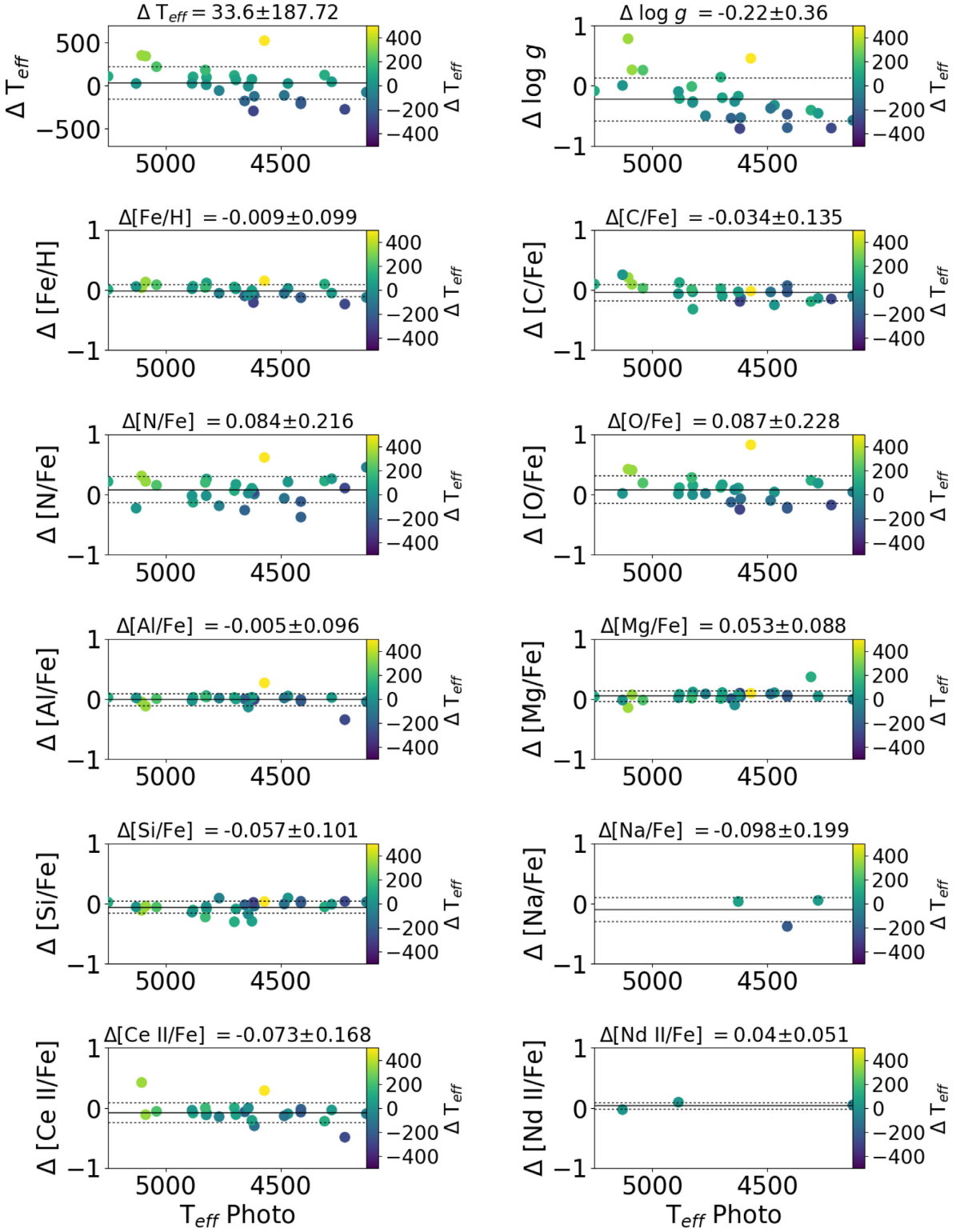

Figure 3. Differences in abundances produced by two runs adopting different temperatures: photometric versus `Payne` APOGEE temperatures; otherwise the same calculation method was employed. The symbols are colour-coded by the differences between the photometric and `Payne` temperatures. The average and ± errors give the standard deviation around the mean of the differences and are listed in the title of each panel.

stars possibly removed from a system merged with our Milky Way (unless they are part of a binary system). We did not detect any variation of the radial velocities that would support the hypothesis that these objects formed through the binary channel, however, most of the stars in our sample were observed just once, and those with multiple observations have a short baseline (<6 months), which makes possible detection of only a small fraction of possible binaries (e.g. Fernández-Trincado et al. 2019a). The radial velocity

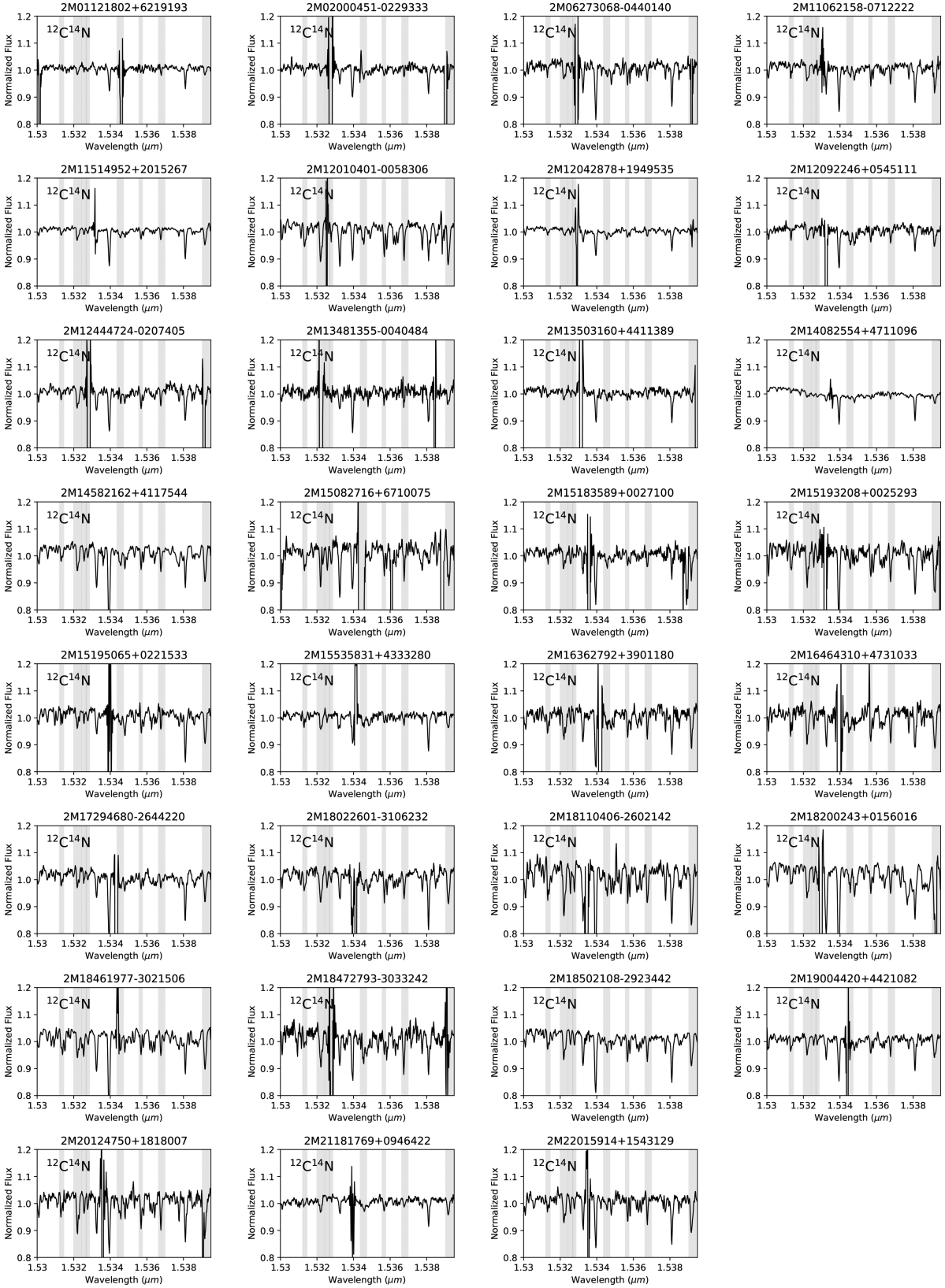

Figure 4. The *H*-band spectra of our N-rich field stars, covering spectral regions around the $^{12}C^{14}N$ band. The grey vertical bands indicate some of the wavelength regimes of the spectral features used in our re-analysis.

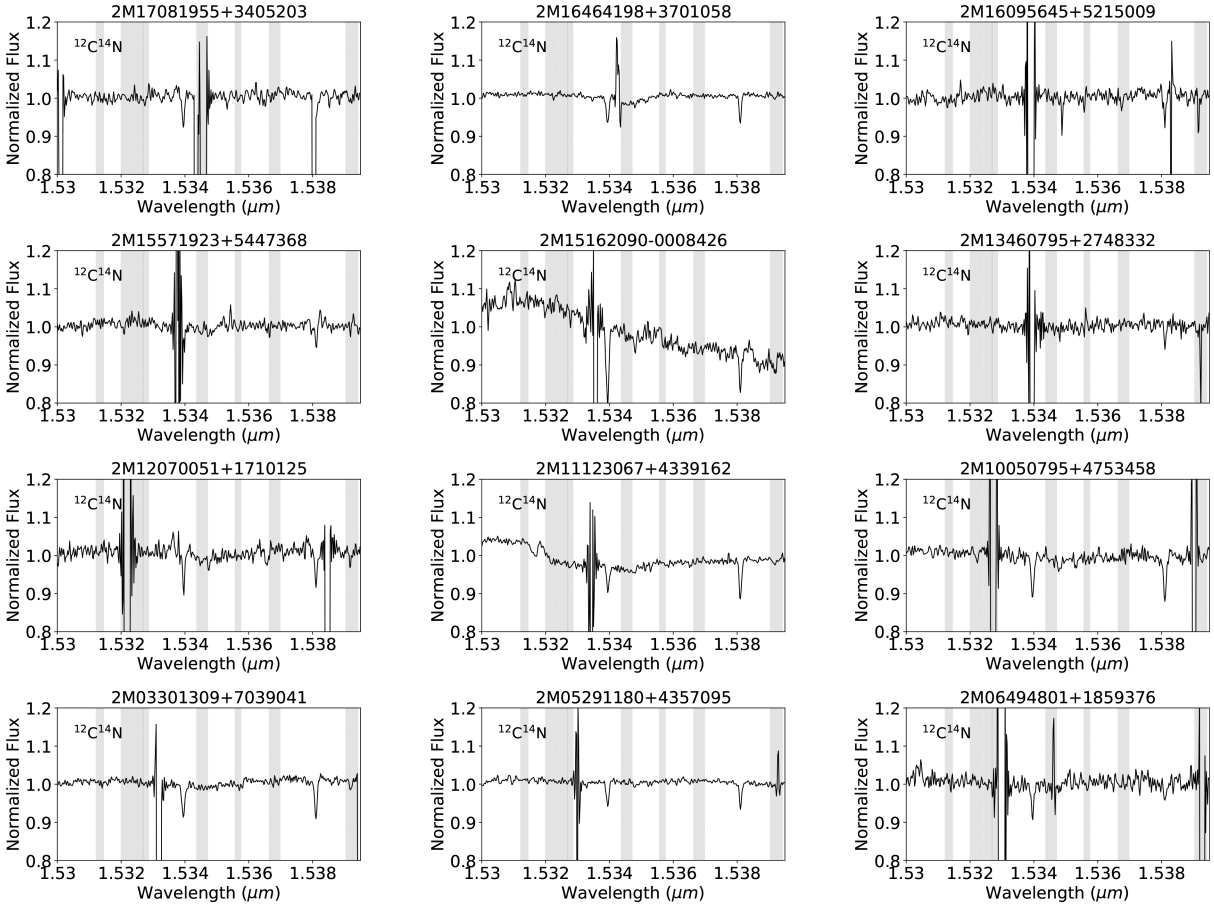

Figure 5. Example of the *H*-band spectra for 12 stars identified as false detections (see the text), covering spectral regions around the $^{12}C^{14}N$ bands. The grey vertical bands indicate some of the wavelength regimes of the spectral features used in our re-analysis.

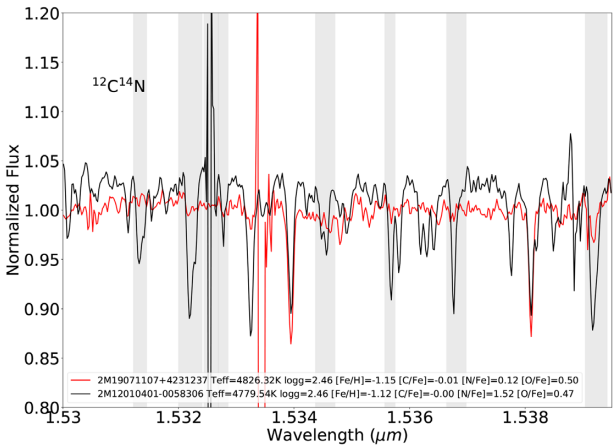

Figure 6. Comparison between the APOGEE spectrum of a normal (red line) and a N-rich (black line) star around the $^{12}C^{14}N$ bands, with similar stellar parameters.

dispersion ($RV_{\rm scatter}$) of our sample is listed in Table 1, which is typically less than 1.5 km s^{-1} over multiple visits, indicating that most of the newly identified N-rich stars are unlikely to be variable stars or part of a binary system.

A small fraction (∼29 per cent) of our giants exhibit large-enrichment in aluminum, [Al/Fe] $\gtrsim +0.5$, which make them more likely to be *migrants* from globular clusters, as they are not typical giants as seen in dwarf galaxy stars (e.g. Hasselquist et al. 2017, 2019). Such N-/Al-rich stars occupy the same locus as *SG*-like N-/Al-rich giants found in previous studies (Fernández-Trincado et al. 2016b, 2017), and the second-generation globular cluster stars (Mészáros et al. 2015; Masseron et al. 2019), reinforcing the similarity between such objects and the globular cluster population. The high levels of Al rule out the possibility that satellite galaxies could have contributed stars to our N-/Al-rich population. These objects exhibit chemical similarities to that the second-generation globular cluster stars, implying that it is possible that a high aluminum and nitrogen abundance could be related to escaped globular cluster stars, or due to metal-poor AGB stars that have experienced strong internal mixing; these chemical properties enable us to classify such objects as *SG-like* (see Table 1). This unique collection of N-rich stars significantly contributes to the task of compiling a more thorough census of anomalously high levels of [N/Fe] and [Al/Fe] throughout the Milky Way, and portends the promising results to be expected from future spectroscopic follow-up observations, and to reconsider the question of *in situ* halo formation (Martell et al. 2016). For other light-element chemical planes, the distinction between the newly identified N-/Al-rich stars and Milky Way population appears to be weaker in Mg and weakest in Si. Here, we show that the [Al/Fe]-[N/Fe] and [Al/Fe]-[Mg/Fe] chemical planes are an especially powerful and reliable diagnostic to identify this unique class of stars among the N-rich population (primarily with metallicities [Fe/H] $\lesssim -0.7$).

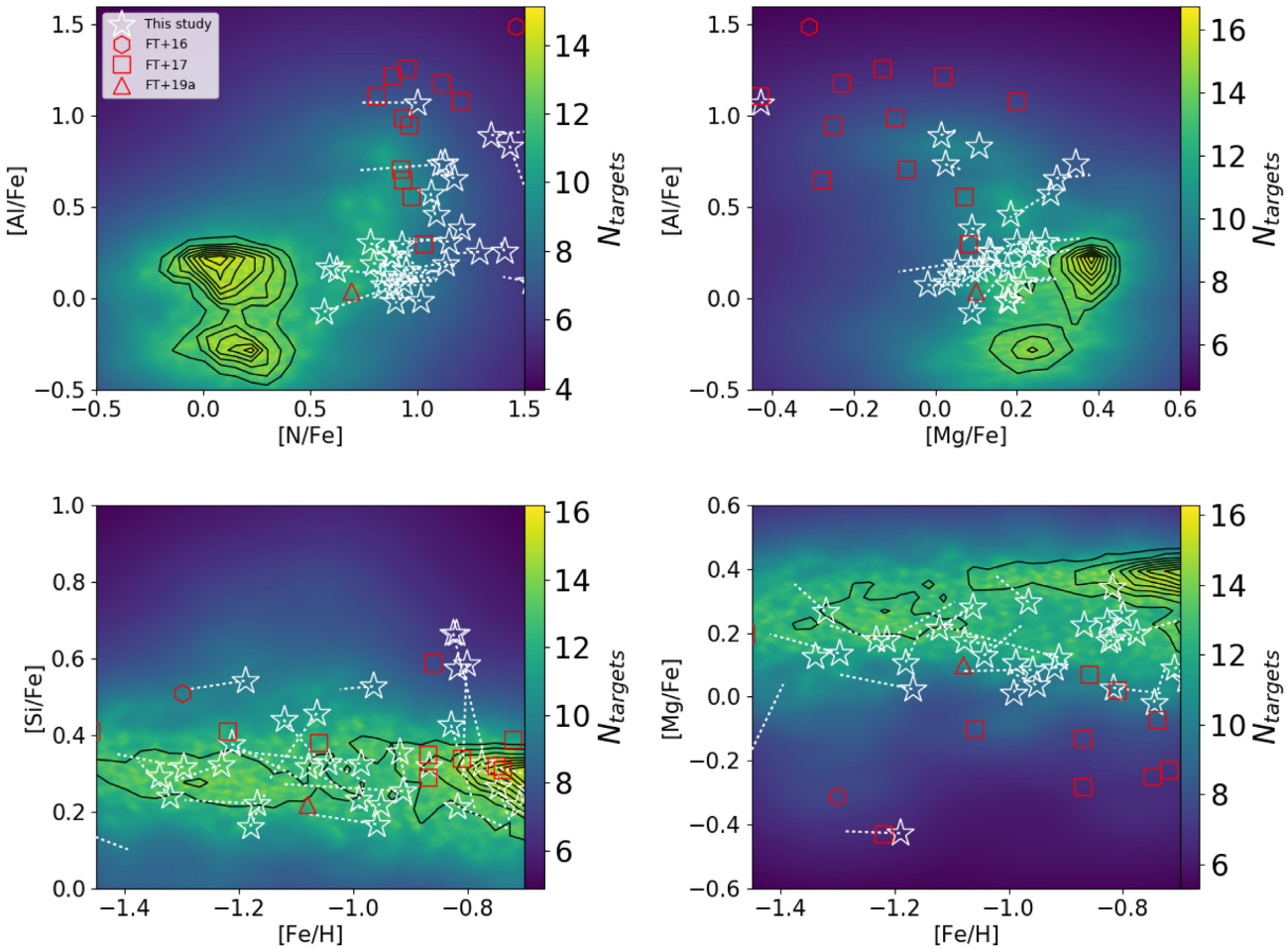

Figure 7. Same as Fig. 1, but for the abundance distribution of the light elements Al, N, Mg, Si, and Fe. The elements for which the newly identified N-rich stars stand out most distinctly from the Milky Way stars are N and Al, where the new stars appear well-separated from the main body of N-normal stars, and less obvious for Si and Mg, with a few exceptions.

At lower [Al/Fe] $\lesssim +0.5$ abundances, there is more overlap in [X/Fe] between the chemistry of Milky Way, dwarf galaxy stars (Hasselquist et al. 2017, 2019), and the so-called first generation of globular cluster stars (Mészáros et al. 2015), i.e. 24 out of 31 N-rich stars in our final data set exhibit chemical abundances that are somewhat distinct in the [Fe/H]-[N/Fe], [Mg/Fe]-[Al/Fe], and [N/Fe]-[Al/Fe] planes, as shown in Fig. 1 and the top panels in Fig. 7, but indistinguishable in other chemical planes from stars having chemistry consistent with the halo and thick disc (*left-bottom panel* in Fig. 7), and are distinctly less Mg-enriched (*right-bottom panel* in Fig. 7). Unfortunately, with only few light-/heavy-elements measured, it is not possible to assign the nucleosynthetic origins of these N-rich/Al-normal stars, and disentangle a dwarf galaxy and globular cluster (stars having peculiar chemical composition like the first population) origins; such objects are classified as *FG-like/dGs* in Table 1. It is likely that they were contributed by different merger events from a dwarf galaxy such as Gaia–Enceladus (Belokurov et al. 2018; Helmi et al. 2018) and the Sagittarius dSph (Hasselquist et al. 2019), or massive disrupted globular clusters (e.g. Kruijssen 2015).

Fig. 8 displays our N-rich sample and globular cluster star data together on the [Al/Fe] versus [Si/Fe], [Mg/Fe], [N/Fe], and [Ce/Fe] planes. The mildly metal-poor globular cluster stars of Masseron et al. (2019), from M5, M107, and M71 are included in this plot, so that the GCs span as wide a metallicity range as our field sample, and have been homogeneously analyzed in the same manner as the N-rich sample presented in this study. Interestingly, the light/heavy elements seen in the globular cluster population match approximately the abundance values determinated for the newly identified N-rich field population at the same [Fe/H]. This result is consistent with findings from other studies, which have characterized SG and FG stars in GCs as having similar chemistry as field stars of same metallicity (e.g. Lind et al. 2015; Martell et al. 2016; Fernández-Trincado et al. 2016b, 2017, 2019a). One obvious exception is the star, 2M15535831 + 4333280, extremely Mg-depleted (<-0.4 dex) and has high [Al/Fe] and [N/Fe] ratios, similar to large light-element enrichment seen in TYC 5619-109-1 (Fernández-Trincado et al. 2016b), which clearly fall within the extreme limits for [Mg/Fe] of the 'second- generation' globular cluster population. Our sample's [N/Fe] appears definitively anomalous, with a spread in [N/Fe] from around 0.5–1.5 dex.

The [O/Fe] abundance ratio is uncertain in the $T_{\rm eff}$ regime of our objects. The uncertainty arises because BACCHUS determines these abundances from the strengths of $^{12}C^{14}N$ and $^{12}C^{16}O$ lines, which become too weak for hotter stars at relatively low metallicities ([Fe/H] $\lesssim -0.7$). Moreover, our results show that, C, Na, Ce II, and Nd II abundances have mostly upper limits (see Table 1), implying that most of these lines become weak and heavily blended to be

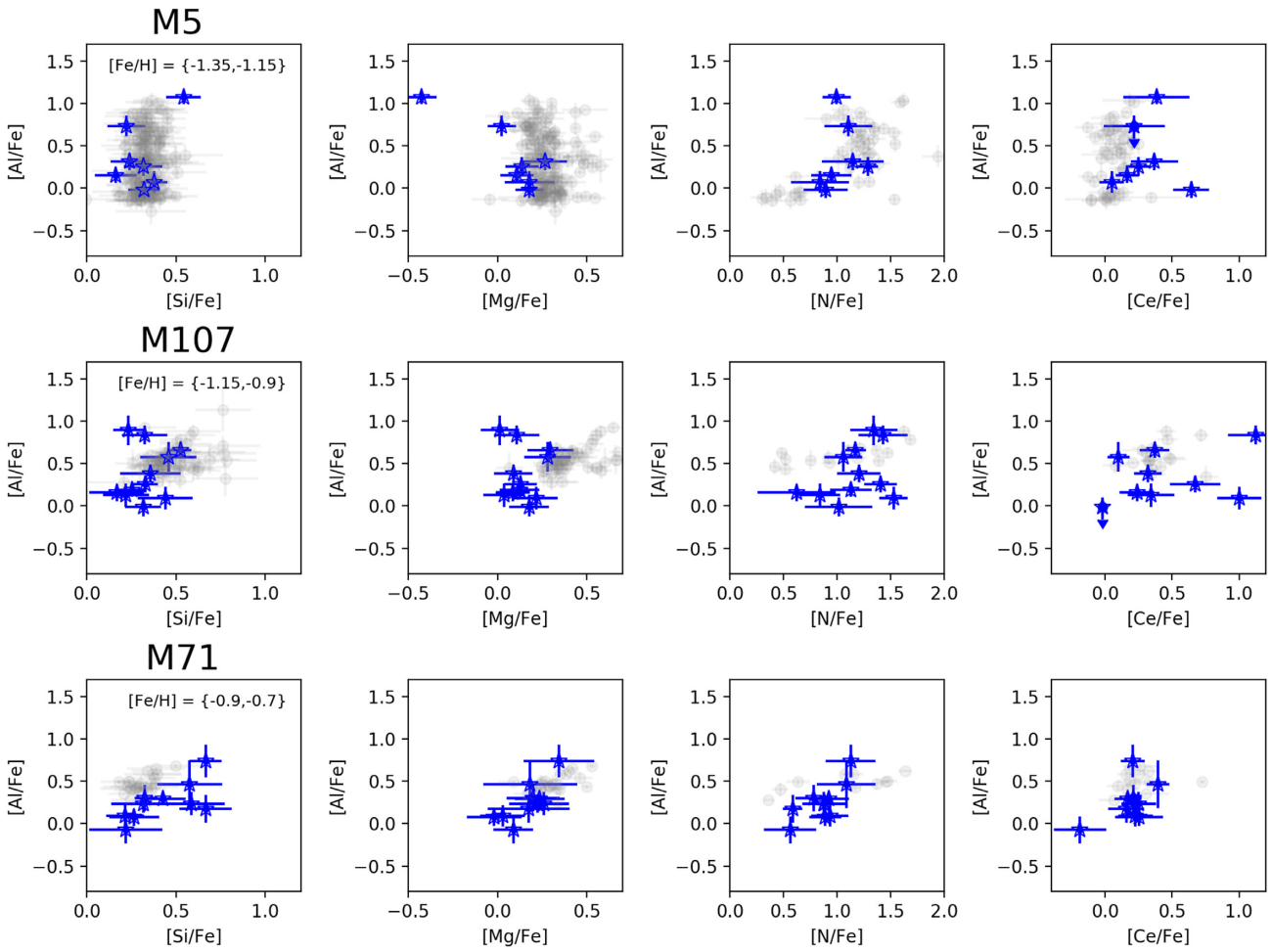

Figure 8. Distribution of [Al/Fe] with light and heavy elements ([Si/Fe], [Mg/Fe], [N/Fe], and [Ce/Fe]). The newly identified N-rich stars are highlighted with blue star symbols, and compared with globular cluster stars from Masseron et al. (2019) of similar metallicity. The chemical abundances provided are the average abundance of selected atomic and molecular lines from our manual inspection with the BACCHUS code.

accurately measured, and therefore the derived abundances strongly depend on the ability of properly reproducing the blend.

3.2 s-process elements

APOGEE has 10 Nd II and 9 Ce II features detectable (Hasselquist et al. 2016; Cunha et al. 2017), however these lines are highly sensitive to stellar parameters, and therefore, only a few can be used to derive upper limits for a large variety of metal-poor stars. In APOGEE spectra, two Na I lines are visible (1.6373 μm and 1.6388 μm) for a few metal-poor stars, however these lines are weak and heavily blended by telluric features at the typical $T_{\rm eff}$ and metallicity for the stars studied in this work. At this time, we cannot guarantee the quality of the abundances for those elements.

The [Ce/Fe] abundance ratios for stars in our sample also show similar levels to those found for stars residing in globular clusters, with a spread in [Ce/Fe] from around −0.2 to ∼1.15. Given the lack of information regarding other neutron-capture elements, it is difficult to assign the nucleosynthetic pathways for such stars, however, we can speculate that the Ce and Nd we have measured are likely to have a pure s-process origin.

3.3 Extra-tidal features around Galactic globular clusters

For most of the newly identified N-rich stars there are no known globular clusters within an angular separation of one degree, except four giants as listed in Table 2 and one potential member of the Ursa Minor Dwarf Spheroidal Galaxy. We find for the first time a N-rich star (2M15183589 + 0027100) that appears likely to be a candidate extra-tidal star (within the errors) associated with Pal 5 based on [Fe/H] metallicity, radial velocity, and elemental abundances. We conclude that 2M15183589 + 0027100 is promising an extra-tidal candidate of Pal 5, which appears to be compatible with the globular cluster escapee scenario, as well as supporting spectroscopic evidence that accretion on to the early Milky Way was significant. For the rest of the three N-rich stars with nearby globular clusters, we find a large spread in metallicity and radial velocity, thus making an extra-tidal origin from nearby GCs for these three N-rich stars very unlikely (see Table 2).

3.4 Possible evolutionary state of the newly identified N-rich stars

Here we qualitatively examine the possible evolutionary state of the newly discovered N-rich stars. To accomplish this, the C, N, O, Mg, Al, Si, Na, Ce II, and Nd II abundances are compared with

Table 2. N-rich giants as tracers of extra-tidal features around Galactic globular clusters and dwarf spheroidal galaxies.

APOGEE−ID	$[Fe/H]_{star}$ [dex]	RV [km s^{-1}]	Nearby object	$[Fe/H]_{gc/Sph}$ [dex]	$RV_{gc/Sph}$ [km s^{-1}]	$r_{t,\,gc/Sph}$ arcmin	Separation arcmin	Extra-tidal N-rich giant Candidates
2M15183589 + 0027100	−1.18	−56.27 ± 0.34	Pal 5	−1.41	−58.6 ± 0.2	16.28	50.7	Likely
2M18110406-2602142	−0.82	−24.96 ± 0.01	NGC 6553	−0.18	0.7 ± 0.4	8.16	25.2	Unlikely
2M15195065 + 0221533	−0.83	−158.58 ± 0.01	NGC 5904	−1.29	53.7 ± 0.3	28.4	25.8	Unlikely
2M16464310 + 4731033	−0.99	−139.80 ± 0.37	NGC 6229 member	−1.47	−138.6 ± 0.8	5.38	2.7	Unlikely
2M15082716 + 6710075	−1.49	−233.13 ± 0.80	Ursa Minor member	...	−246.9[a]	...	5.14	Unlikely

Note: [a]McConnachie (2012).

Table 3. Abundance determination sensitivity to the stellar parameters from our present measurements.

APOGEE−ID	X	$\sigma_{[X/H],T_{eff}}$	$\sigma_{[X/H],\,logg}$	$\sigma_{[X/H],\xi_t}$	σ_{mean}	σ_{total}
2M01121802 + 6219193	Fe	0.048	0.010	0.015	0.102	0.114
2M01121802 + 6219193	C	0.011	0.085	0.117	0.315	0.347
2M01121802 + 6219193	N	0.158	0.092	0.138	0.169	0.285
2M01121802 + 6219193	O	0.134	0.027	0.012	0.051	0.147
2M01121802 + 6219193	Mg	0.061	0.041	0.025	0.022	0.082
2M01121802 + 6219193	Al	..	..	..	..	..
2M01121802 + 6219193	Si	..	..	..	..	..
2M01121802 + 6219193	Ce	0.054	0.090	0.098	..	0.144
2M01121802 + 6219193	Nd	..	..	..	..	..
2M01121802 + 6219193	Na	..	..	..	..	..

Note: Table 4 is published in its entirety via CDS. A portion is shown here for guidance regarding its form and content. The reported uncertainty for each chemical species in column 7 is: $\sigma_{total} = \sqrt{\sigma^2_{[X/H],T_{eff}} + \sigma^2_{[X/H],logg} + \sigma^2_{[X/H],\xi_t} + \sigma^2_{mean}}$.

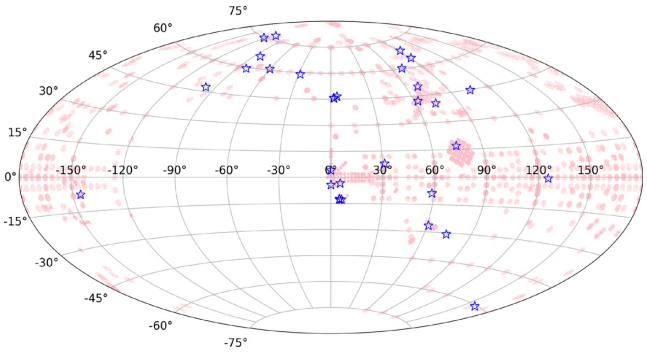

Figure 9. Aitoff projection map in Galactic coordinates for the APOGEE giants used in this work (pink dots). The newly identified N-rich giants are highlighted with blue unfilled 'star' symbols.

theoretical AGB nucleosynthesis predictions: FRUITY[2] models from Cristallo et al. (2015), which we have compared to observations with the FRUITY models of metallicity $Z = 2 \times 10^{-3}$, the Monash model of metallicity [Fe/H] = −1.2 from Fishlock et al. (2014), and the ATON model ([Fe/H] = −1.2) from Ventura et al. (2016), as shown in Fig. 10. Based on χ^2 fitting of the light/heavy elements, we find that the majority of our N-rich stars fit the metal-poor, low-mass (M <1.5 – 5 $M_\odot$) AGB yields from Cristallo et al. (2015), which dominates the production of s-process elements (Ce II and Nd II) in most of the cases, but is at odds with the carbon abundance of the FRUITY database. On the other hand, the more massive AGB nucleosynthesis ATON and Monash models in the range of M > 5–7 $M_\odot$ is in better agreement with the observations, with the exception of [O/Fe], which shows a significant deviation from the theoretical predictions, perhaps due to the fact that the abundance of [O/Fe] is uncertain in the T_{eff} regime studied here. An alternative origin to produce high nitrogen abundance could be ascribed to strong internal mixing process, which would suggest that most of the newly identified N-rich stars could probably be evolved objects, possibly in an 'early-AGB' or AGB phase. However, a future inventory of the chemistry of these stars, in particular the elements involved in the neutron-capture reactions (e.g. Pereira et al. 2017, 2019b), would be crucial to understand the origin of these unique objects.

[2]FUll-Network Repository of Updated Isotopic Tables and Yields: http://fruity.oa-abruzzo.inaf.it/

3.5 Orbits

In order to provide insight on the origin of our stars across the Milky Way, the positional information of the newly identified N-rich stars was combined with precise proper motions from *Gaia* DR2 (Arenou et al. 2018; Lindegren et al. 2018), radial velocity from the APOGEE-2 survey (Nidever et al. 2015; Majewski et al. 2017), and the newly measured spectrophotometric distances from Leung & Bovy (2019) as input data for the new state-of-the-art orbital integration package gravpot16.[3] Orbits are integrated in both an axisymetric model, and a model including the perturbations due to a realistic (as far as possible) rotating 'boxy/peanut' bar, which fits the structural and dynamical parameters of the Galaxy to the best we know of the recent knowledge of our Milky Way (José G. Fernández-Trincado et al., in preparation). Supplementary Figs A1 and A2 show the orbits for each individual star, using as initial conditions the central values, both in the case of the axisymmetric potential in the inertial Galactic frame of reference (column 1) and the model with bar (columns 2, 3, and 4) assuming four different values of the angular velocity of the bar $\Omega_{bar} = 35, 40, 45$, and 50 km s^{-1} kpc^{-1}, with a bar mass of 1.1×10^{10} $M_\odot$, and a present-day angle orientation of 20º, in the *noninertial* frame (where the bar is at rest). For each star, we plotted the projection of the orbit on the Galactic plane (X–Y) and on the meridional plane (R– Z).

To model the uncertainty distributions, we sampled a half million orbits using a simple Monte Carlo scheme, assuming a normal distribution for the uncertainties of the input parameters (positions, distance, radial velocity, and proper motions). The results are listed in Table 4; the data presented in this table correspond to a backward time integration of 3 Gyr in our dynamical model. Fig. 11 shows

[3]For guidance, the Galactic convention adopted by this study is: X-axis is oriented toward $l = 0^\circ$ and $b = 0^\circ$, and the Y-axis is oriented toward $l = 90^\circ$ and $b = 0^\circ$, and the disc rotates toward $l = 90^\circ$; the velocities are also oriented in these directions. In this convention, the Sun's orbital velocity vector is $[U_\odot, V_\odot, W_\odot]$ = [11.1, 12.24, 7.25] km s^{-1} (Brunthaler et al. 2011). The model has been rescaled to the Sun's Galactocentric distance, 8.3 kpc, and the local rotation velocity of 239 km s^{-1}.

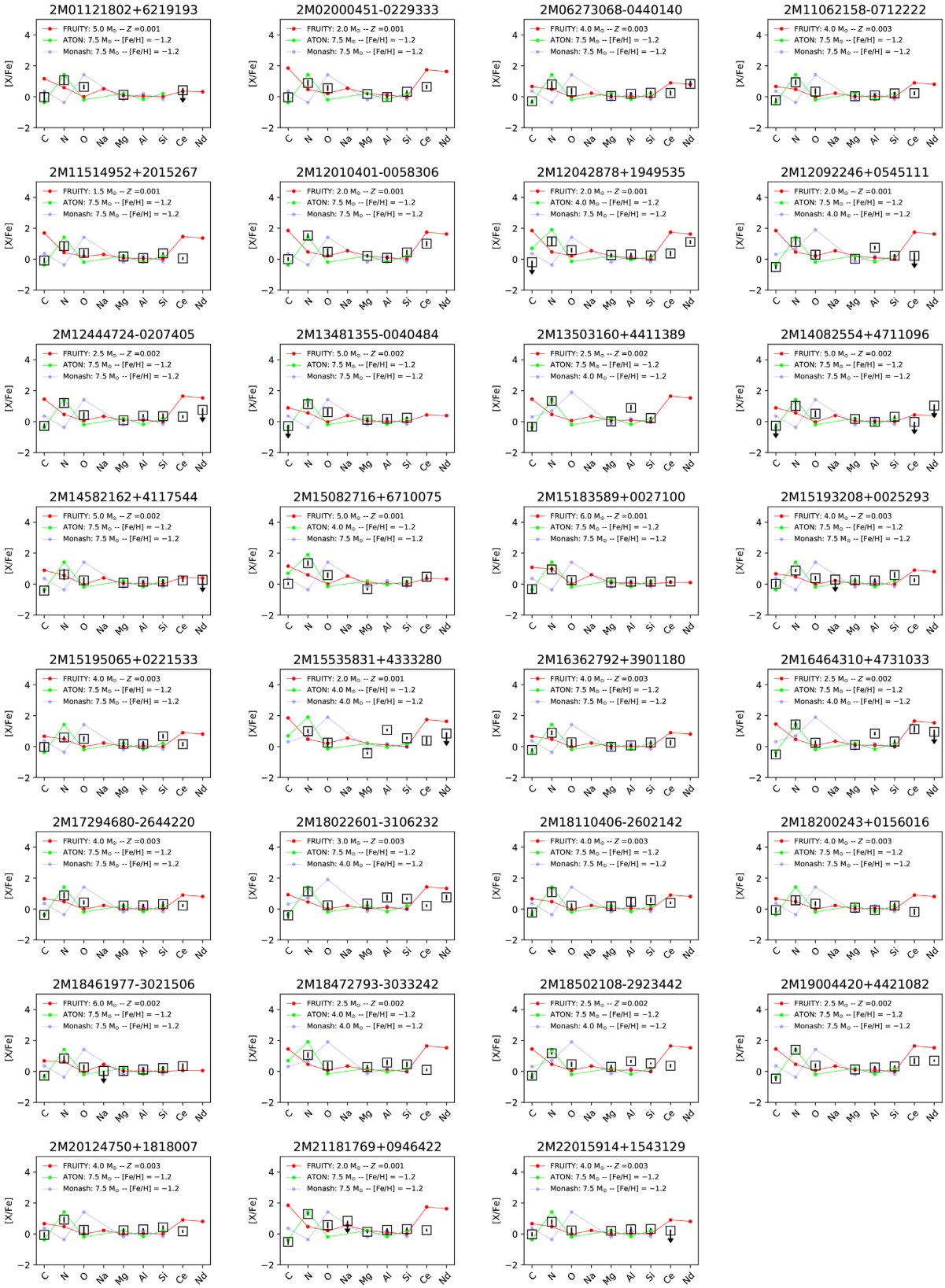

Figure 10. Chemical abundances for the 31 N-rich stars. Each determined abundance is shown as a black dot, and solid arrows represent measurements where only an upper limit was possible. The error bars are estimates of the uncertainties in our measurements as listed in Table 3. These abundances are compared to three synthetic AGB yields that best fit the observed data; for a selection of the $Z = 0.001$ (FRUITY; red dots and solid line) and −1.2 dex (ATON; green dots and solid line, and Monash; blue dots and solid line) models.

Table 4. Orbital elements obtained using a simple Monte Carlo approach for the 31 N-rich stars. The average value of the orbital elements (pericentric and apocentric radii, the eccentricity, the maximum distance the orbit reaches above/below the Galactic plane, as well as the maximum and minimum of the z-component of the angular momentum in the inertial frame, L_z) was found for the half million realizations, with uncertainty ranges given by the 16th *(subscript)* and 84th *(superscript)* percentile values.

Ω_{bar} km s^{-1} kpc^{-1}	APOGEE–ID	RA ($^\circ$)	Dec. ($^\circ$)	$RV \pm \Delta$ km s^{-1}	$d \pm \Delta$ kpc	$\mu_\alpha \pm \Delta$ mas yr^{-1}	$\mu_\delta \pm \Delta$ mas yr^{-1}	$\langle r_{\rm min}\rangle$ kpc	$\langle r_{\rm max}\rangle$ kpc	$\langle e\rangle$	$\langle Z_{\rm max}\rangle$ kpc	$\langle L_{z,\,\rm min}\rangle$ km s^{-1} kpc^{-1}	$\langle L_{z,\,\rm max}\rangle$ km s^{-1} kpc^{-1}
35	2M01121802 + 6219193	18.075 099	62.322 044	-256.06 ± 0.07	4.02 ± 0.39	5.369 ± 0.031	-1.376 ± 0.035	$0.05^{0.10}_{0.02}$	$11.73^{12.04}_{11.51}$	$0.99^{0.99}_{0.98}$	$0.37^{0.40}_{0.35}$	$-9.0^{0.0}_{-15.0}$	$11.0^{21.0}_{7.0}$
40								$0.06^{0.10}_{0.02}$	$12.59^{12.70}_{11.48}$	$0.99^{0.99}_{0.98}$	$0.37^{0.40}_{0.35}$	$-15.0^{-5.0}_{-20.0}$	$9.0^{18.0}_{3.0}$
45								$0.05^{0.12}_{0.02}$	$12.29^{13.49}_{11.86}$	$0.99^{0.99}_{0.97}$	$0.39^{0.44}_{0.36}$	$-12.0^{-10.0}_{-24.0}$	$4.0^{12.0}_{-4.0}$
50								$0.09^{0.18}_{0.04}$	$13.81^{14.02}_{13.50}$	$0.98^{0.99}_{0.97}$	$0.37^{0.42}_{0.36}$	$-26.0^{-13.0}_{-35.0}$	$7.0^{21.0}_{-1.2}$
35	2M02000451 − 0229333	30.018 804	−2.492 584	68.68 ± 0.19	7.89 ± 1.13	3.701 ± 0.076	-4.492 ± 0.048	$1.28^{2.27}_{0.36}$	$14.45^{15.38}_{13.69}$	$0.83^{0.95}_{0.71}$	$11.62^{15.23}_{8.79}$	$-56.0^{-14.0}_{-93.0}$	$-45.0^{-2.0}_{-84.0}$
40								$1.11^{2.13}_{0.39}$	$14.84^{15.68}_{13.98}$	$0.86^{0.94}_{0.73}$	$11.74^{15.05}_{8.99}$	$-56.0^{-17.0}_{-96.0}$	$-39.0^{-7.0}_{-78.0}$
45								$1.09^{2.00}_{0.33}$	$14.25^{15.13}_{13.76}$	$0.85^{0.95}_{0.74}$	$11.64^{14.68}_{8.83}$	$-54.0^{-14.0}_{-94.0}$	$-37.0^{1.0}_{-72.0}$
50								$1.15^{2.20}_{0.38}$	$14.25^{17.16}_{13.64}$	$0.85^{0.95}_{0.72}$	$11.30^{15.38}_{9.17}$	$-59.0^{-20.8}_{-93.0}$	$-41.0^{-5.8}_{-81.0}$
35	2M06273068 − 0440140	96.877 869	−4.670 57	66.63 ± 0.06	7.94 ± 1.05	-0.260 ± 0.046	-0.057 ± 0.045	$13.27^{14.19}_{12.38}$	$15.86^{17.10}_{14.67}$	$0.08^{0.09}_{0.08}$	$1.28^{1.56}_{1.05}$	$-339.0^{-317.0}_{-362.0}$	$-339.0^{-317.0}_{-361.0}$
40								$13.24^{14.18}_{12.40}$	$15.89^{17.15}_{14.65}$	$0.09^{0.10}_{0.08}$	$1.28^{1.56}_{1.05}$	$-339.0^{-317.0}_{-362.0}$	$-339.0^{-317.0}_{-362.0}$
45								$13.26^{14.16}_{12.34}$	$15.89^{17.19}_{14.69}$	$0.09^{0.09}_{0.08}$	$1.28^{1.56}_{1.05}$	$-339.0^{-317.0}_{-362.0}$	$-339.0^{-317.0}_{-362.0}$
50								$13.25^{14.18}_{12.35}$	$15.90^{17.15}_{14.68}$	$0.09^{0.10}_{0.08}$	$1.28^{1.56}_{1.05}$	$-339.0^{-317.0}_{-362.0}$	$-339.0^{-317.0}_{-362.0}$

Note: Table 5 is published in its entirety via CDS. A portion is shown here for guidance regarding its content.

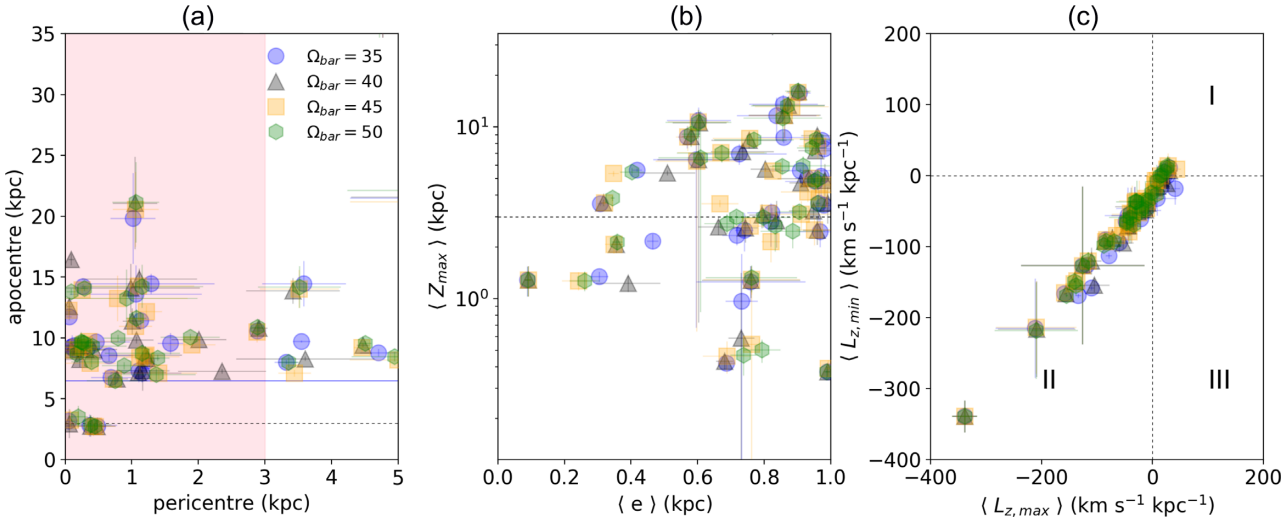

Figure 11. Orbital parameters calculated with different pattern speed of the bar, 35 (blue circles), 40 (grey triangles), 45 (orange squares), and 50 (green hexagons) km s^{-1} kpc^{-1}. In panel (a) the shaded region and the black dotted line indicates the radius (i.e. 3 kpc; Barbuy, Chiappini & Gerhard 2018) of the Milky Way bulge, while the blue line indicates the location of the bar's corotation radius (*CR* ∼ 6.5 kpc). For panel (a) a star below the black dotted line would have a bulge-like orbit, and in panel (b) the black dotted line represents the edge Z_{max} of the thick disc (∼3 kpc; Carollo et al. 2010). In panel (c), the black dotted lines divide the regions with prograde orbits (*region II*) with respect to the direction of the Galactic rotation, retrograde orbits (*region I*), and stars that have prograde–retrograde orbits at the same time (*region III*). The error bars show the uncertainty in the computed orbital parameters.

a scatter plot of all the possible combinations among the orbital elements in the non-axisymmetric potential model. We see that, in each panel, most the stars are grouped in two regions, indicating that they likely belong to the same component. In this case, one group is confined to the bulge/bar, and a second group is apparently moving outwards from the co-rotation (CR) region.

The newly identified N-rich stars are found to have radial and prograde orbits, with pericenter values less than 3 kpc (inside the bulge region), apocenter values ranging between 6.5 and5 8 kpc, orbital eccentricities larger than 0.5, and maximum vertical excursions from the Galactic plane ranging between 0.5 and 58 kpc. The orbital parameters clearly show that a few these stars live in the inner Galaxy, while most are in the inner halo of the Milky Way. Fig. 9 shows the Aitoff project of our objects, which reveals that 6 out of 31 of our stars are located toward the bulge region, 2M17294680−2644220, 2M18022601−3106232, 2M18110406−2602142, 2M18461977−3021506, 2M18472793−3033242, and 2M18502108−2923442; from this group we found that the orbital properties of three of them suggest that they are actually halo interlopers into the inner Galaxy (2M17294680−2644220, 2M18461977−3021506, and 2M18502108−2923442), while the other three stars appear to have bulge/bar-like prograde orbits. It is very likely that such N-rich stars trapped into the bulge/bar potential could be linked to merger debris of surviving globular clusters in bulge/bar-like orbits, such as M 62 (see e.g. Minniti et al. 2018).

It is also worth mentioning that there are two other N-rich stars, 2M15535831 + 4333280 (*SG-like*), 2M16362792 + 3901180 (*FG-like/dGs*), whose orbits are retrograde with respect to the direction of the Galactic rotation. We found that the abundance patterns of such stars, namely the α-elements, neutron-capture elements, and the abundance ratios of [Al/Fe], most resemble the known chemical signature of globular cluster stars. The chemistry and dynamical behaviour of this sub-sample of N-rich stars suggest that they could be the debris of dissipated globular clusters, indicating that there may be a significant population of these peculiar abundance giants residing in the Galactic field.

Lastly, 26 out of 31 N-rich stars appear to behave as halo-like orbits, intriguingly in the prograde sense with respect to the rotation of the bar, suggesting that they were likely formed during the very early stages of the evolution of the Galaxy (e.g. Khoperskov et al. 2018), in a similar way as Galactic globular clusters. It is important to note that prograde orbits have been observed before in the inner halo (Bonaca et al. 2017; Hayes et al. 2018; Fernández-Alvar et al. 2019; Lucey et al. 2019), as well as for other globular clusters (Moreno, Pichardo & Velázquez 2014; Pérez-Villegas et al. 2018), however this is not yet well-understood. We also found that most of the simulated orbits are situated in the inner Galaxy, which means that most of the N-rich stars are on highly eccentric orbits (with eccentricities greater than 0.6), reaching out to a maximum distance from the Galactic plane larger than 3 kpc. On the other hand, a handful of the N-rich stars have energies allowing the star to move inwards from the bar's corotation radius (<6.5 kpc). In this region, a class of orbits appears around the Lagrange points on the minor axis of the bar that can be stable, and have a banana-like shape parallel to the bar, as illustrated in a few cases in Fig. A1, while the orbits liberating around Lagrange points aligned with the bar are unstable and are probably chaotic orbits. Our model naturally predicts trajectories indicating that most of the N-rich stars are confined to the Galactic halo.

Additionally, in Table 4 and Fig. 11 we show the variation of the z-component of the angular momentum (L_z), as a function of $\Omega_{\rm bar}$. Since this quantity is not conserved in a model like `GravPot16` (with non-axisymmetric structures), we follow the change, $\{-L_z, +L_z\}$, where negative L_z in our reference system means that the cluster orbit is prograde (in the same sense as the disc rotation). Both prograde and prograde–retrograde orbits with respect to the direction of the Galactic rotation are clearly revealed for a few cases, this effect is strongly produced by the presence of the Galactic bar, further indicating a chaotic behaviour.

A major limitation of the employed dynamical model is that it ignores secular changes in the Milky Way potential over time, which might be important in understanding of the evolution in the inner Galaxy. An in-depth analysis of such dynamical effects is beyond the scope of this paper, however, the adopted technique shows that the inclusion of a more realistic (as far as possible) bar potential is essential for the description of the dynamical behaviour of N-rich stars in the innermost part of the Galaxy.

4 CONCLUDING REMARKS

We have taken advantage of the fist `Payne` data release of APOGEE abundances, which determine best-fitting stellar parameters and abundances using neural networks as an emulator. We applied a series of quality cuts on the initial `Payne` catalogue, ensuring that the data have sufficiently high-quality spectra needed to estimate chemical abundances for a wide range of chemical species, as well as re-examined line-by-line each APOGEE spectrum with the `BACCHUS` pipeline. Our study presents a unique collection of 31 newly identified N-rich stars towards the bulge and inner halo of the Milky Way that exhibit anomalously high levels of [N/Fe] over a narrow range of metallicities ($-1.5 \lesssim$[Fe/H]$\lesssim -0.7$), below the metal-poor tail of the thick-disc metallicity distribution. Based on their [Al/Fe] abundance ratios, we classified them into two groups, the N-/Al-rich giant-stars ([Al/Fe] $\gtrsim +0.5$) with chemical signatures similiar to second-generation globular cluster stars, and a second group, the N-rich/Al-normal ([Al/Fe] $< +0.5$) with chemistry similar to the first generation of stars seen in Galactic globular clusters and the population of stars in dwarf galaxies. For many of them, we determined, for the first time the abundances of s-process elements (Ce II and Nd II).

We did not detect any significant variation of their radial velocities that would support the hypothesis of mass transfer, however most of the chemical species examined, along with the high nitrogen abundances could support the idea that the process responsible for the stars can be qualitatively explained by massive evolved objects, possibly 'early-AGB' or AGB stars. We hypothesize that massive ($M > 5$–$7\ M_{\odot}$) AGB stars may produce a [N/Fe] over-abundance in some of our N-rich giant stars within the Milky Way. However, more detailed AGB nucleosynthesis models, as well as more observations, will be necessary to confirm or refute the scenario related to AGB stars. Combining our abundance results, orbital analysis, and the absence of radial velocity variations, we conclude that most of the newly identified objects are associated with the bulge/bar structure and the inner Galactic halo, and are likely escaped members of small satellites that were tidally disrupted and captured by the Milky Way.

ACKNOWLEDGEMENTS

The author is grateful for the enlightening feedback from the anonymous referee. We thank Szabolcs Mészáros for helpful support computing the photometry $T_{\rm eff}$, and especially grateful for the technical expertise and assistance provided by the Instituto de Astrofísica de Canarias (IAC). We are grateful to Sarah L. Martell, for helpful discussions. This article is based upon work from the 'ChETEC' COST Action (CA16117), supported by COST (European Cooperation in Science and Technology). J.G.F-T is supported by FONDECYT No. 3180210. J.G.F-T acknowledges the use of `TOPCAT` (Taylor 2005) through out the course of this investigation. T.C.B. acknowledge partial support for this work from grant PHY 14-30152; Physics Frontier Center / JINA Center for the Evolution of the Elements (JINA-CEE), awarded by the US National Science Foundation. B.T. acknowledges support from the one-hundred-talent project of Sun Yat-Sen University. S.L-M acknowledges funding from the Australian Research Council through Discovery grant DP180101791, and from the UNSW Scientia Fellowship program. Parts of this research were conducted by the Australian Research Council Centre of Excellence for All Sky Astrophysics in 3 Dimensions (ASTRO 3D), through project number CE170100013. APV acknowledges an FAPESP for the postdoctoral fellowship grant no. 2017/15893-1 and the DGAPA-PAPIIT grant IG100319.

`BACCHUS` have been executed on computers from the Utinam Institute of the Université de Franche-Comté, supported by the Région de Franche-Comté and Institut des Sciences de l'Univers (INSU).

Funding for the `gravpot16` software has been provided by the Centre national d'études spatiales (CNES) through grant 0101973 and UTINAM Institute of the Université de Franche-Comté, supported by the Région de Franche-Comté and Institut des Sciences de l'Univers (INSU). Simulations have been executed on computers from the Utinam Institute of the Université de Franche-Comté, supported by the Région de Franche-Comté and Institut des Sciences de l'Univers (INSU), and on the supercomputer facilities of the Mésocentre de calcul de Franche-Comté.

Funding for the Sloan Digital Sky Survey IV has been provided by the Alfred P. Sloan Foundation, the U.S. Department of Energy Office of Science, and the Participating Institutions. SDSS- IV acknowledges support and resources from the Center for High-Performance Computing at the University of Utah. The SDSS web site is www.sdss.org. SDSS-IV is managed by the Astrophysical Research Consortium for the Participating Institutions of the SDSS Collaboration including the Brazilian Participation Group, the Carnegie Institution for Science, Carnegie Mellon University, the Chilean Participation Group, the French Participation Group, Harvard-Smithsonian Center for Astrophysics, Instituto de Astrofìsica de Canarias, The Johns Hopkins University, Kavli Institute for the Physics and Mathematics of the Universe (IPMU)/University of Tokyo, Lawrence Berkeley National Laboratory, Leibniz Institut für Astrophysik Potsdam (AIP), Max-Planck-Institut für Astronomie (MPIA Heidelberg), Max-Planck-Institut für Astrophysik (MPA Garching), Max-Planck-Institut für Extraterrestrische Physik (MPE), National Astronomical Observatory of China, New Mexico State University, New York University, University of Dame, Observatório Nacional/MCTI, The Ohio State University, Pennsylvania State University, Shanghai Astronomical Observatory, United Kingdom Participation Group, Universidad Nacional Autónoma de México, University of Arizona, University of Colorado Boulder, University of Oxford, University of Portsmouth, University of Utah, University of Virginia, University of Washington, University of Wisconsin, Vanderbilt University, and Yale University.

REFERENCES

Abolfathi B. et al., 2018, ApJS, 235, 42
Alvarez R., Plez B., 1998, A&A, 330, 1109
Arenou F. et al., 2018, A&A, 616, A17
Asplund M., Grevesse N., Sauval A. J., 2005, in Barnes T. G., III, Bash F. N., eds, ASP Conf. Ser. Vol. 336, Cosmic Abundances as Records of Stellar Evolution and Nucleosynthesis, Astron. Soc. Pac., San Francisco, p. 25
Barbuy B., Chiappini C., Gerhard O., 2018, ARA&A, 56, 223
Bastian N., Lardo C., 2018, ARA&A, 56, 83
Belokurov V., Erkal D., Evans N. W., Koposov S. E., Deason A. J., 2018, MNRAS, 478, 611
Blanton M. R. et al., 2017, AJ, 154, 28

Bonaca A., Conroy C., Wetzel A., Hopkins P. F., Kereš D., 2017, ApJ, 845, 101
Bressan A., Marigo P., Girardi L., Salasnich B., Dal Cero C., Rubele S., Nanni A., 2012, MNRAS, 427, 127
Brunthaler A. et al., 2011, Astron. Nachr., 332, 461
Carollo D. et al., 2010, ApJ, 712, 692
Carollo D., Martell S. L., Beers T. C., Freeman K. C., 2013, ApJ, 769, 87
Cristallo S., Straniero O., Piersanti L., Gobrecht D., 2015, ApJS, 219, 40
Cui X.-Q. et al., 2012, Res. Astron. Astrophys., 12, 1197
Cunha K. et al., 2017, ApJ, 844, 145
Deng L.-C. et al., 2012, Res. Astron. Astrophys., 12, 735
Fernández-Alvar E. et al., 2019, MNRAS, 487, 1462
Fernández-Trincado J. G. et al., 2015b, A&A, 583, A76
Fernández-Trincado J. G. et al., 2016b, ApJ, 833, 132
Fernández-Trincado J. G. et al., 2017, ApJ, 846, L2
Fernández-Trincado J. G. et al., 2018, preprint (arXiv:1801.07136)
Fernández-Trincado J. G. et al., 2019a, preprint (arXiv:1902.10635)
Fernández-Trincado J. G. et al., 2019b, preprint (arXiv:1904.05884)
Fernández-Trincado J. G., Vivas A. K., Mateu C. E., Zinn R., Robin A. C., Valenzuela O., Moreno E., Pichardo B., 2015a, A&A, 574, A15
Fernández-Trincado J. G., Robin A. C., Reylé C., Vieira K., Palmer M., Moreno E., Valenzuela O., Pichardo B., 2016a, MNRAS, 461, 1404
Fishlock C. K., Karakas A. I., Lugaro M., Yong D., 2014, ApJ, 797, 44
García Pérez A. E. et al., 2016, AJ, 151, 144
Gilmore G. et al., 2012, The Messenger, 147, 25
González Hernández J. I., Bonifacio P., 2009, A&A, 497, 497
Grevesse N., Scott P., Asplund M., Sauval A. J., 2015, A&A, 573, A27
Gunn J. E. et al., 2006, AJ, 131, 2332
Gustafsson B., Edvardsson B., Eriksson K., Jørgensen U. G., Nordlund Å., Plez B., 2008, A&A, 486, 951
Harris W. E., 1996, AJ, 112, 1487
Hasselquist S. et al., 2016, ApJ, 833, 81
Hasselquist S. et al., 2017, ApJ, 845, 162
Hasselquist S. et al., 2019, ApJ, 872, 58
Hawkins K., Masseron T., Jofré P., Gilmore G., Elsworth Y., Hekker S., 2016, A&A, 594, A43
Hayes C. R. et al., 2018, ApJ, 852, 49
Helmi A., Babusiaux C., Koppelman H. H., Massari D., Veljanoski J., Brown A. G. A., 2018, Nature, 563, 85
Holtzman J. A. et al., 2015, AJ, 150, 148
Holtzman J. A. et al., 2018, AJ, 156, 125
Ibata R. A., Malhan K., Martin N. F., 2019, ApJ, 872, 152
Jönsson H. et al., 2018, AJ, 156, 126
Karinkuzhi D., Goswami A., 2015, MNRAS, 446, 2348
Kemp A. J. et al., 2018, MNRAS, 480, 1384
Khoperskov S., Mastrobuono-Battisti A., Di Matteo P., Haywood M., 2018, A&A, 620, A154
Koch A., Grebel E. K., Martell S. L., 2019, A&A, 625, A75
Kruijssen J. M. D., 2015, MNRAS, 454, 1658
Leung H. W., Bovy J., 2019, preprint (arXiv:1902.08634)
Lind K. et al., 2015, A&A, 575, L12
Lindegren L. et al., 2018, A&A, 616, A2
Lucey M. et al., 2019, preprint (arXiv:1903.11615v2)
Luo A.-L. et al., 2012, Res. Astron. Astrophys., 12, 1243
Majewski S. R. et al., 2017, AJ, 154, 94
Majewski S. R., Zasowski G., Nidever D. L., 2011, ApJ, 739, 25
Martell S. L. et al., 2016, ApJ, 825, 146
Martell S. L., Grebel E. K., 2010, A&A, 519, A14
Martell S. L., Smolinski J. P., Beers T. C., Grebel E. K., 2011, A&A, 534, A136
Masseron T. et al., 2019, A&A, 622, A191
Masseron T., Merle T., Hawkins K., 2016, BACCHUS: Brussels Automatic Code for Characterizing High accUracy Spectra, Astrophysics Source Code Library, record ascl:1605.004
McConnachie A. W., 2012, AJ, 144, 4
Mészáros S. et al., 2015, AJ, 149, 153
Minniti D., Fernández-Trincado J. G., Ripepi V., Alonso-García J., Contreras Ramos R., Marconi M., 2018, ApJ, 869, L10
Moreno E., Pichardo B., Velázquez H., 2014, ApJ, 793, 110
Nidever D. L. et al., 2015, AJ, 150, 173
Pereira C. B., Smith V. V., Drake N. A., Roig F., Hasselquist S., Cunha K., Jilinski E., 2017, MNRAS, 469, 774
Pereira C. B., Drake N. A., Roig F., 2019a, MNRAS, 488, 482
Pereira C. B., Holanda N., Drake N. A., Roig F., 2019b, AJ, 157, 70
Pérez-Villegas A., Rossi L., Ortolani S., Casotto S., Barbuy B., Bica E., 2018, Publ. Astron. Soc. Aust., 35, e021
Plez B., 2012, Turbospectrum: Code for spectral synthesis, Astrophysics Source Code Library. record ascl:1205.004
Randich S., Gilmore G., Gaia-ESO Consortium, 2013, The Messenger, 154, 47
Recio-Blanco A. et al., 2017, A&A, 602, L14
Schiavon R. P. et al., 2017a, MNRAS, 465, 501
Schiavon R. P. et al., 2017b, MNRAS, 466, 1010
Smith V. V. et al., 2013, ApJ, 765, 16
Tang B., Liu C., Fernández-Trincado J. G., Geisler D., Shi J., Zamora O., Worthey G., Moreno E., 2019, ApJ, 871, 58
Taylor M. B., 2005, in Shopbell P., Britton M., Ebert R., eds, ASP Conf. Ser. Vol. 347, Astronomical Data Analysis Software and Systems XIV. Astron. Soc. Pac., San Francisco, p. 29
Ting Y.-S., Conroy C., Rix H.-W., Cargile P., 2019, ApJ, 879, 69
Ventura P., Stanghellini L., Di Criscienzo M., García-Hernández D. A., Dell'Agli F., 2016, MNRAS, 460, 3940
Zamora O. et al., 2015, AJ, 149, 181
Zasowski G. et al., 2013, AJ, 146, 81
Zasowski G. et al., 2017, AJ, 154, 198
Zhao G., Zhao Y.-H., Chu Y.-Q., Jing Y.-P., Deng L.-C., 2012, Res. Astron. Astrophys., 12, 723

SUPPORTING INFORMATION

Supplementary data are available at *MNRAS* online.

Figure A1. Orbits for the newly identified N-rich stars in an x–y projection, integrated adopting the central values (positions, proper motions, radial velocity, and distance) in both an axisymmetric model (column 1) and a model including the Galactic bar potential in the *non-inertial* reference frame where the bar is at rest (columns 2, 3, 4, and 5). The green solid line shows the size of the Galactic bar, and the large green circle the co-rotation radius, CR∼6.5 kpc. The small red square symbol marks the present position of the star, and the blue star symbol marks its final position.
Figure A2. Orbits for the same sample in an R–z projection. The symbols have the same meaning as those in Fig. A1.

Please note: Oxford University Press is not responsible for the content or functionality of any supporting materials supplied by the authors. Any queries (other than missing material) should be directed to the corresponding author for the article.

This paper has been typeset from a TEX/LATEX file prepared by the author.